

pubs.acs.org/macroletters Viewpoint

100th Anniversary of Macromolecular Science Viewpoint: Polymeric Materials by *In Situ* Liquid-Phase Transmission Electron Microscopy

Lucas R. Parent, Karthikeyan Gnanasekaran, Joanna Korpanty, and Nathan C. Gianneschi*



Cite This: ACS Macro Lett. 2021, 10, 14-38

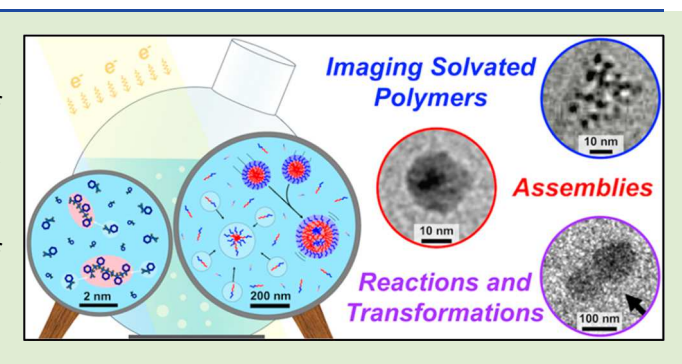


ACCESS

III Metrics & More

Article Recommendations

ABSTRACT: A century ago, Hermann Staudinger proposed the macromolecular theory of polymers, and now, as we enter the second century of polymer science, we face a different set of opportunities and challenges for the development of functional soft matter. Indeed, many fundamental questions remain open, relating to physical structures and mechanisms of phase transformations at the molecular and nanoscale. In this Viewpoint, we describe efforts to develop a dynamic, *in situ* microscopy tool suited to the study of polymeric materials at the nanoscale that allows for direct observation of discrete structures and processes in solution, as a complement to light, neutron, and X-ray scattering methods. Liquid-phase transmission electron microscopy (LPTEM) is a



nascent *in situ* imaging technique for characterizing and examining solvated nanomaterials in real time. Though still under development, LPTEM has been shown to be capable of several modes of imaging: (1) imaging static solvated materials analogous to cryo-TEM, (2) videography of nanomaterials in motion, (3) observing solutions or nanomaterials undergoing physical and chemical transformations, including synthesis, assembly, and phase transitions, and (4) observing electron beam-induced chemical-materials processes. Herein, we describe opportunities and limitations of LPTEM for polymer science. We review the basic experimental platform of LPTEM and describe the origin of electron beam effects that go hand in hand with the imaging process. These electron beam effects cause perturbation and damage to the sample and solvent that can manifest as artefacts in images and videos. We describe sample-specific experimental guidelines and outline approaches to mitigate, characterize, and quantify beam damaging effects. Altogether, we seek to provide an overview of this nascent field in the context of its potential to contribute to the advancement of polymer science.

INTRODUCTION

The level of complexity that has been achieved in modern polymeric nanomaterials and the advancements enabled by living polymerization reactions, in particular, have benefited greatly from advancements in characterization tools. Despite myriad novel, functional polymeric materials that have been developed over the past 100 years, we continue to seek a deeper understanding of the basic mechanisms and pathways by which they form and how we can control these processes to develop products with specific physical properties and functionalities. Therefore, we believe that *in situ* characterization of solvated nanoscale materials via direct microscopy methods holds great promise for polymer science in the next century. However, realizing this promise remains a significant challenge.

Solvated polymeric nanomaterials that contain numerous individual nanostructures are currently most effectively characterized by harnessing an array of bulk solution- or surface-scattering methods. Such techniques are highly developed and powerful for analyzing polymers and soft matter in general.¹⁻⁴ However, bulk scattering techniques

require fitting ensemble data to models and thus only describe the average physical form of the collection of structures in the sample, not necessarily the actual form of any individual structure. Direct physical characterization, or imaging, by comparison provides a real space image or description of the specific physical form of individual nanostructures in the sample. However, many of these direct methods are inherently limited by low sampling statistics and are prone to observational and experimental artefacts. Transmission electron microscopy (TEM), operating in the 50–300 keV energy range, is one of the few direct techniques able to achieve the nanometer resolution necessary to image nanomaterials. However, with the exception of modern environmental

Received: August 14, 2020 Accepted: November 9, 2020



TEM, this technique demands that the sample holder be confined to a small volume and held at ultrahigh vacuum (UHV) (Figure 1).¹⁰ We note that there are other potential

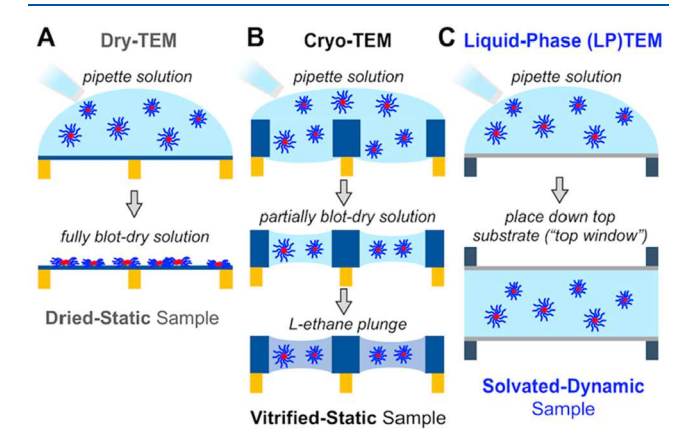


Figure 1. Comparison of the sample preparation for the three main TEM techniques used for solvated polymer samples (solutions). (A) Dry-TEM: the sample solution is drop-cast on an ultrathin C-film grid and is then completely dried. (B) Cryo-TEM: the sample solution is drop-cast on a thick, holey C-substrate grid, then partially dried to a thin liquid layer with filter paper, and plunged into l-ethane, becoming vitrified. (C) In situ liquid-phase (LP)TEM: the sample solution is drop cast on a thin, robust substrate, or "window" (a-Si₃N $_x$ or graphene), and then sealed between a second window, forming a "liquid cell".

imaging techniques outside of the scope of this review, each with its own set of opportunities and artefacts, including atomic force microscopy, ^{11–13} ion microscopy, ¹⁴ and synchrotron X-ray microscopy. ^{15–17}

Typically, TEM samples are prepared in the dry state, as dried droplets cast on a thin substrate, and consequently, any solvated polymer sample is prone to drying artefacts that can alter its native structure (Figure 1A). TEM has taken an increasingly prominent role in polymer science with the development and widespread adoption of cryogenic-TEM (cryo-TEM), where the solution-phase sample is vitrified, not dried, and imaged in that state, free from drying artefacts (Figure 1B). 1,5-9 Though it provides detailed morphological information, cryo-TEM can have its own sample preparation artefacts, and it limits a microscopist to observing a necessarily static sample, capturing a snapshot at one point in time. Thus, cryo-TEM is inherently incapable of capturing discrete dynamic processes in a continuous fashion, relying on aliquoted sample preparation as with dry-state TEM. Most relevant to the polymeric and soft matter field, cryo-TEM is largely limited to aqueous samples with a few exceptions. 1,18 Moreover, despite efforts to plunge vitrify samples that are initially at elevated temperatures, this has proven unreliable, with cryo-TEM largely limited to the study of samples at room temperature at the time of vitrification. Samples that have temperature-specific morphologies cannot be accurately visualized by cryo-TEM. This is also true for dry-state TEM, where evaporation is additionally confounding.

In true liquid-phase TEM (*in situ* LPTEM) characterization, the sample is neither dried nor vitrified but instead is maintained fully solvated in its native media and its native temperature (Figure 1C).²⁰ In theory, this allows the system under investigation to be fully dynamic in time, enabling *in situ* videographic observations of chemical and materials processes

and the continuous tracking of interactions and transformations of individual nanoscale objects. In its most basic mode, single-exposure imaging, LPTEM can be used to observe solvated but otherwise static particles. In this static imaging mode, we can determine the morphology of discrete polymeric structures. Employed in this manner, LPTEM avoids the potential artefacts associated with cryo-TEM sample preparation that can complicate the understanding of samples under study, such as ice crystal formation, inhomogeneous vitrification, or morphological transitions during vitrification. 5-9 LPTEM also allows for the analysis of solvated structures in organic or highly viscous solvents or other nonaqueous media, which remain technically challenging in cryo-TEM preparation. In addition, recently developed variable-temperature (VT) LPTEM allows the sample solution to be maintained and imaged at elevated temperatures, enabling the observation of phases or structures that form only above room temperature, which is generally not possible by cryo-TEM as noted above. ^{21,22} In short, in this most basic case, LPTEM expands the possibilities for systems that can be imaged on the nanoscale to include systems at elevated temperatures and nonaqueous systems.

Above all, it is the ability of LPTEM to continuously record dynamic processes over time that truly transcends other TEM methods for studying solvated polymer samples. This has especially high potential for the study of chemical reactions that lead to the formation and transformation of nanostructures. Using LPTEM, individual polymer chains or nanostructures can be observed continuously in time, which is not possible by even the best time-series cryo-TEM experiment. where each individual structure is static within the time series, and the mechanism of a given transition or reaction can only be inferred using prior knowledge and complementary bulk in situ scattering data (light, neutron, or X-ray). 1-4,11,23-26 Unlike conventional bulk scattering techniques, LPTEM does not suffer from averaging or modeling effects that can distort the data. 1-4 This is both a strength and a potential weakness. The lack of sampling statistics in LPTEM data makes any one LPTEM dataset especially susceptible to experimental and observational artefacts, while the data obtained reflects discrete structures and processes. 20,27 As with any analytical method, if we are able to understand and account for the experimental artefacts that complicate LPTEM data, specifically effects from electron (e⁻) beam irradiation and spatial confinement within the necessarily small solution cells used, we can reliably contextualize the data obtained and properly interpret the results. LPTEM observation requires the scattering of electrons by the sample to generate a signal, which will also inherently alter a polymer specimen and its solvent. It is these competing features of the electron beam in any LPTEM experiment that will form the basis of our discussion in this Viewpoint.

For LPTEM to impact polymer science, we are mainly interested in studying processes relevant to what actually occurs in a benchtop reaction vessel. Any artefactually altered processes or structures specific to an arbitrary imaging modality may be of little import. In this Viewpoint, we aim to provide a unified, generalized description of the sample vessel performance during LPTEM experimentation, highlight potential artefactual effects specific to the LPTEM vessel and imaging conditions used, and suggest means to minimize or eliminate these artefacts to extract meaningful data. The goal is to develop an experimental technique capable of truly mimicking bulk-like conditions while conducting *in situ*,

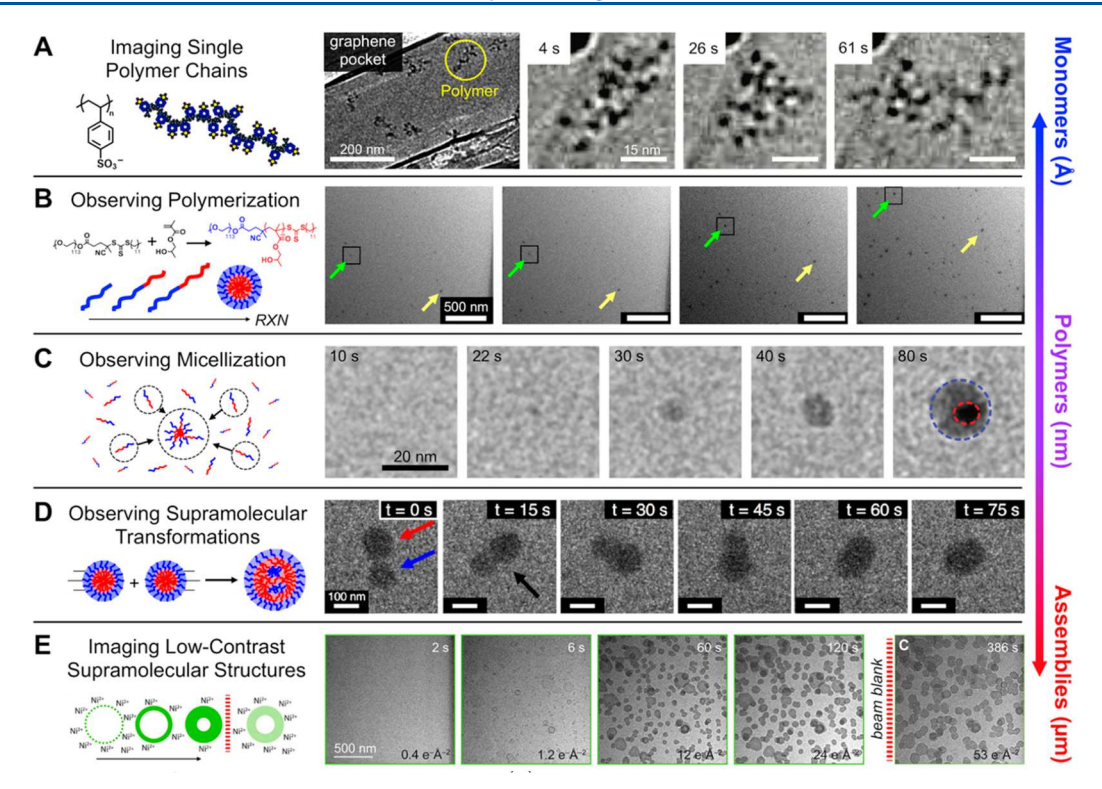


Figure 2. Examples of LPTEM applied to study polymer science. (A) Imaging individual polymer chains using graphene-LCTEM. Reproduced with permission from ref 55. Copyright 2017 Wiley-VCH. (B) *In situ* LPTEM time lapse of e-beam induced polymerization of monomers. Reproduced with permission from ref 57. Copyright 2018 ACS Publications. (C) *In situ* LCTEM video of the micellization of a copolymer (EO₁₀₀-PO₆₅-EO₁₀₀) solution. Reproduced with permission from ref 59. Copyright 2019 Royal Society of Chemistry. (D) *In situ* LCTEM video of micellemicelle fusion, which can be tracked in time to quantify the fusion process and capture the internalization of solvent that occurs. Reproduced with permission from ref 46. Copyright 2017 ACS Publications. (E) *In situ* staining of low-contrast liposomes in LPTEM using 1 mM NiCl₂. Reproduced with permission from ref 62. Copyright 2020 ACS Publications.

nanoscale observations of solvated polymers and their nanostructures. To begin, we review the literature of LPTEM applied to polymeric samples, highlighting examples where control of LPTEM experimental conditions was successfully harnessed to mitigate artefacts or damage to the systems under study, giving insight into the property of the materials themselves.

■ PIONEERING EXAMPLES OF LPTEM STUDIES OF SOFT MATTER ASSEMBLIES AND POLYMERIC MATERIALS

While the study of robust, inorganic materials, such as metallic or ionic crystals, has been the largest focus of study by far for this nascent technique, 20,28,37-39,29-36 the study of polymers and organic materials using LPTEM has been comparatively limited. 40,41 This is because soft materials are considered a challenge due to their inherent sensitivity to e-beam-induced radiation damage and their poor TEM contrast generally, which is even lower in liquid media. However, this has begun to change as polymeric and organic materials are being more commonly studied, as experimental techniques for sample preparation, image capture, and image analysis are improved (Figure 2). 41,42,51,43-50 LPTEM applied to solvated organic nanostructures was first demonstrated by Mirsaidov et al. in 2012,⁴² demonstrating that using low electron flux TEM conditions, similar to those employed for proteins in cryo-TEM, it was possible to statically image protein nanostructures, specifically ca. 100 nm wide crystalline acrosomal bundles at sub-3 nm resolution, in water using LPTEM at

low total fluence in TEM mode. ⁴² This was quickly followed by Evans et al., who imaged sub-20 nm ferritin nanoparticles and nanolipoprotein disks in buffered water at ca. 2 nm resolution in STEM. ⁵² For clarity, electron flux is in units of e⁻/Å²s, while fluence is the cumulative number of total incident electrons applied, in e⁻/Å². We note that LPTEM applied to biological soft matter has been an active area of development in parallel to that of solvated polymers, and we point to recent reviews on LPTEM of biological systems, which have similar but distinct experimental challenges. ⁵³,54

Proetto et al. reported the first study of dynamics and motion of individual amphiphilic block copolymer supramolecular nanoassemblies captured by LPTEM.⁵¹ Here, Pt centers were coordinated to norbornyl monomers to increase the scattering contrast of the micellar assemblies in aqueous solution, giving these ca. 150 nm polymer nanoparticles high contrast over the pure water background at the imaging conditions used. At the molecular level, Nagamanasa et al. demonstrated the ability to video the conformation of individual polymer unimers in water and track their dynamic motion and molecular degradation under TEM irradiation using ultrathin graphene windows (Figure 2A). 55 By applying object tracking and video quantification to LPTEM data of dynamic polymeric nano-objects, it has been determined that the diffusion and motion of solvated nanostructures during LPTEM is often anomalous from bulk Brownian behavior. This anomalous motion is influenced by window-surface effects, the e- irradiation, and the frame rate of acquisition. 27,46,51 Indeed, subdiffusive anomalous motion has been

observed in multiple polymer systems in LPTEM, where the specific motion of individual micelles videoed during LPTEM has been used to understand the forces and conditions within the liquid cell vessel.^{27,46,51}

Beyond videoing basic motion of polymer chains or nanostructures in solution, LPTEM has also been applied to study the nucleation, assembly, and transformation of polymeric nanostructures, as well as the formation and evolution of individual polymer chains. LPTEM has been shown to be uniquely capable of studying this class of processes. Liu et al. demonstrated the first in situ polymerization of monomers using an LPTEM system with electrochemical capabilities, driving the micron-scale electrodeposition of poly(3,4-ethylenedioxythiophene) (PEDOT) on an electrode surface from an aqueous EDOT solution under continuous observation. ⁵⁶ In this early work, the authors were unable to verify the molecular structure of the electrodeposited material by post mortem characterization, leaving open the possibility of the structures formed being related to a beam damage product.⁵⁶ Touve et al. reported the first in situ polymerization of amphiphilic diblock copolymers observed by LPTEM, using a polymer system where the TEM beam creates a chemical environment that mimics the condition of bulk polymerization.⁵⁷ They determined that e-beam-induced radiolysis of the aqueous solution, containing monomers and radical chain transfer agents, drives monomer polymerization in solution via reversible addition-fragmentation chain transfer (RAFT). The polymerization in turn triggers the formation of micelles, here ca. 50 nm diameter particles, that are comparable to those prepared by bulk synthesis via polymerization-induced self-assembly (PISA, Figure 2B). Here, systematic damage control tests were performed to determine low flux and fluence imaging conditions where PISA was not detectably affected by the TEM beam. However, again, the molecular structure of the in situ formed polymers was not verified by a post mortem analysis method.

To date, post mortem validation of polymer structures formed by in situ polymerization during LPTEM has been limited to 2D polymers that form highly crystalline nanoparticles during polymerization, which provide precise, dry-TEM diffraction patterns. 21,58 Smith et al. demonstrated the first use of variable-temperature (VT) LPTEM (at 80 °C) to observe the thermal polymerization of hexahydroxytriphenylene (HHTP) and phenylenebis(boronic acid) (PBBA) monomers in a purely organic solvent solution, a blend of mesitylene, dioxane, acetonitrile, and methanol, and the resulting formation of ca. 25 nm diameter COF-5 colloidal nanoparticles using stroboscopic, low fluence in situ imaging.² The polymeric colloidal crystals formed in situ and the monomer solutions were both highly susceptible to beam damage artefacts at 80 °C. Post mortem dry-TEM diffraction of the COF-5 particles was critical to verify their true structural identity, with beam damage products similarly identified by diffraction analysis following the liquid-phase electron microscopy experiments.

Li et al. first captured micellization to form nanoassemblies using LPTEM and an aqueous solution of preformed polymeric amphiphiles (Figure 2C). Based on the difference in contrast between the core and corona blocks of the sub-50 nm diameter spherical micelles that formed, which could be tracked and quantified, assembly kinetics and pathways were determined for different system conditions with or without Au nanoparticles. In an earlier study, Parent et al. used *in situ*

LPTEM to observe preformed, kinetically trapped block copolymer micelles, initially ca. 20 nm in diameter, in buffered water, undergoing both unimer addition and particle-particle fusion events to grow into larger, ca. 40-150 nm diameter, assemblies with complex internal structures. 46 Correlating the in situ LPTEM data with in silico models, fusion was found to be associated with the internalization of additional solvent within the micelles, leading to a phase transition from spherical to bicontinuous morphology (Figure 2D). LPTEM has also been used to visualize micelle assembly via liquid-liquid phase separation—a phenomenon of high importance in living cells and synthetic supramolecular systems. Ianiro et al. observed that individual unimers of an amphiphilic diblock copolymer dispersed in acetone before solvent exchange with water prompts the formation of polymer-rich liquid droplet phases, which serve as the seeds for molecular organization and micelle transformation into ca. 150 nm diameter vesicles with ca. 20 nm membrane thickness.⁴⁵ These LPTEM data reveal the role of phase separation in vesicle formation, an experimental finding that was strengthened by self-consistent field computations and Gibbs free energy calculations. 45 The thermal fragmentation of preformed block copolymer micelles in an ionic liquid has also been observed by LPTEM using an "open" LPTEM platform (see next section). 60 Early et al. found that the fragmentation of ca. 100 nm diameter spherical micelle assemblies occurs by their transformation into elongated "peanut"-shaped morphologies, followed by necking, neck thinning, and ultimately separation into two smaller micelles.

In all of these LPTEM examples, imaging polymeric nanomaterials has been a challenge, largely due to their inherently low contrast in TEM. Generally, polymer structures in the range of ca. 25 nm up to ca. 500 nm are best suited for study by LPTEM; smaller structures can yield prohibitively low contrast in water, and larger structures begin to significantly degrade imaging resolution due to sample thickness. One route to enable easier imaging of polymer nanostructures in liquid was demonstrated by Piffoux et al., where the electron-beaminduced reduction of chloroauric acid to yield ca. 5 nm Au metal nanoparticles resulted in metal deposition on the membranes of extracellular vesicles, ca. 100 nm in diameter. This "metal tagging" served to increase the contrast of the vesicles relative to the liquid background. However, using this method, the strong interaction between the Au nanoparticles and the liquid-cell windows led to subdiffusive motion and further aggregation of the extracellular vesicles. Advancing the concept of an in situ stain, Gnanasekaran et al. demonstrated liquid-phase staining of phospholipid unilamellar vesicles of ca. 100 nm diameter with thin membranes using a metal cation (Ni²⁺) that preferentially adsorbs to negatively charged moieties on the liposomes (Figure 2E).62 The increased scattering cross section of the metal cation in the liposome membrane led to staining of the liposome nanostructures. This phenomenon was partially reversible and heavily dependent on the concentration of the metal cation and electron dose conditions. In situ staining techniques will generally find utility for static observation of the physical structure and morphology of low contrast polymer samples, as it will necessarily alter the physicochemical properties and dynamic behavior of the sample and the structures observed.

Despite these precedents, LPTEM is inherently destructive, and polymeric materials are among the most sensitive to observational artefacts and damage. In a traditional benchtop

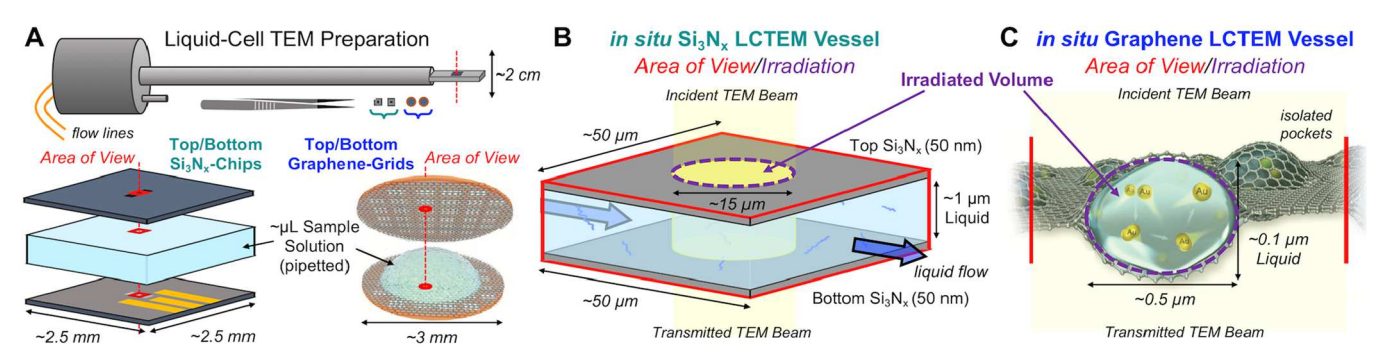


Figure 3. Diagram of window-based liquid-cell TEM. (A) LCTEM holders are designed to accommodate LCTEM chips (Si substrate with thin a-Si₃N_x windows) or graphene grids which (B/C) hermetically seal the sample solution (pLs) in the holder tip from the UHV column. Inlet/outlet flow lines allow external solutions to be injected into the "liquid-cell" region using a-Si₃N_x windows. (B) The Si₃N_x chips have etched-out window regions that align to create the LCTEM vessel and area of view (marked in red). (C) In graphene LCTEM, the sample solution is sealed into small isolated pockets between two thin graphene films, which reduces the area of view in the graphene liquid-cell vessel. Reproduced with permission from ref 77. Copyright 2017 Wiley-VCH.

polymer chemistry experiment, for example, synthesizing and measuring the viscosity of a novel hydrogel, we have a good understanding of the metadata that contextualizes the viscosity data obtained: the chemical properties of the sample including polymer concentration, solvent, temperature, pH, and additive concentrations and the type of viscosity probe required for accurate calibration. In an in situ LPTEM experiment by comparison, the sample's basic metadata is potentially convoluted by multiple and interrelated artefacts specific to the LPTEM conditions. If we hope to study processes of relevance to polymer science using LPTEM and contextualize the in situ data we obtain, we must understand and ideally quantify these additional artefacts. This requires an understanding of how polymer samples and chemistries are damaged or altered during LPTEM operation. In the following sections, we break down the path of the incident electron beam though the liquid-cell vessel loaded with a polymer sample solution and highlight the various ways in which the beam can either directly or indirectly alter natural polymer chemistries or structures. Our goal is to both provide strategies for effectively using LPTEM for polymeric samples and give caution regarding the potential to misinterpret artefactual LPTEM data.

■ LPTEM VESSEL: A NANO- TO MICROSCALE REACTION VESSEL

Here, we consider the liquid-cell a unique vessel for conducting solution-phase chemical processes (Figure 3). The LPTEM experimental system is highly complex, due to both the nano-to-microscale spatial geometry of the vessel and the ever-present irradiation by the TEM beam. These factors play a role in reactions and reactivity as well as in the motion of the materials in what is certainly distinct from any standard benchtop reaction vessel. The LPTEM technique has been developed by multiple research groups and instrumentation manufacturers working largely in parallel. As a result, several different in situ LPTEM platforms have been established, falling into one of two types: (A) windowless sample holders ("open"-LPTEM) where the sample solution is open to the UHV of the TEM column, similar to a cryo-TEM sample, as shown in Figure 1B, or the far more common (B) windowbased sample holders that hermetically seal and confine the solution between thin solid membranes, creating a "liquid-cell" (LCTEM) that is isolated from the column UHV (Figure 1C

and Figure 3). 20,33,63 Open-LPTEM requires sample solutions with very low vapor pressures that do not evaporate rapidly under UHV, such as certain ionic liquids. Consequently, samples that can be effectively studied using open environmental chamber LPTEM are limited. However, for applicable systems, the quality, in terms of contrast and resolution, of in situ imaging data will be high, as windows used to confine the solution necessarily lower the achievable contrast and resolution and can undergo undesired interactions with the sample. The first in situ open-LPTEM study of polymer nanostructures in an ionic liquid has been recently reported for observing the fragmentation of micelles. 60 The bulk polymerization and crosslinking of ionic liquid monomers due to e-beam irradiation has also been demonstrated using liquid-phase scanning electron microscopy (LPSEM), suggesting that ionic liquids themselves can be highly sensitive to direct radiolysis degradation.⁷² Recently, the use of an environmental-TEM (ETEM) to create free-standing water droplets on thin carbon TEM grids using saturated water vapor has opened the possibility of using ETEM for open-LPTEM studies of hydrated polymers in pure water in the future.7

In general, solvated polymeric samples exist in aqueous or organic media, and currently, window-based platforms must be used, of which there are two main types: (1) amorphous-Si₃N_x windows used with commercial LCTEM holders and (2) home-made graphene window liquid cells (and recently, hybrids that combine graphene and $a-Si_3N_x$ or other substrates). ^{20,33,63,74-76} Each LCTEM platform has its own advantages and limitations in terms of imaging performance and unwanted interactions with the sample, which we discuss in the following sections. Regardless of the window material and sample, the basic experimental platform of LCTEM remains fundamentally the same; the sample solution, confined to ca. sub-micron liquid thickness and containing solvated nanostructures, monomers, or polymer chains, is enclosed between two thin windows, which have a thickness ranging from a single monolayer of graphene up to ca. 50 nm thick a-Si₃N_r (Figure 3). For commercial LCTEM platforms (Figure 3A), Si support chips with etched-out "electron transparent" a-Si₃N_x windows are used to confine the sample solution, which is hermetically sealed from the column vacuum in the tip of a "liquid-cell" holder by an O-ring system (Figure 3A,B). Graphene-based liquid cells that use TEM grids as a support are not commercially available, and we point to several recent

reviews on the various preparation methods for using graphene windows for LCTEM (Figure 3C).^{74,77–81} The viewing region, marked in red in Figure 3, is the region where top and bottom windows align and overlap. It is generally referred to as the "liquid-cell" (LC), as this is the only region of the LCTEM vessel that we can directly observe once the sample is sealed and in the electron microscope (Figure 3C). This region is ca. $50 \times 50 \,\mu\text{m}^2$ for a-Si₃N_x windows or ca. 500 nm \times 500 nm² for graphene windows depending on the pocket size. We note that, generally, in graphene-LCTEM, due to the small size of each isolated pocket, typically a sub-micron diameter, the entire volume of the solution is confined to remain continually under direct TEM beam irradiation (purple in Figure 2B). Conversely, the larger volume and flowlines of the liquid cell in Si₃N_x-LCTEM allow for the diffusion of solution molecules into and out of the region of direct TEM beam irradiation. This will alter the in situ radiolysis chemistries when using graphene- or Si₃N_x-LCTEM for a given sample.

In general, any LC-vessel will have an exceptionally large window surface area per volume of solution. For TEM in the 50–300 kV range, imaging is only possible through liquids that are at most several microns thick and, more realistically, for resolving low-Z organic structures, through submicron thickness. Under these liquid thickness constraints, no location within the LC-vessel is ever further than several hundred nanometers from the window surface, and a significant fraction of the solution volume is within the outer Helmholtz layer of a window surface. Indeed, chemical and molecular interactions that occur at a window—solution interface tend to dominate in LCTEM experiments, and we must be acutely aware of the effects that the windows, in combination with the e-beam, can have on systems under study. 20,27,28

To start, we first consider the initial state of the liquid-cell windows prior to TEM beam irradiation. Amorphous silicon nitride (a-Si₃N_x) membranes have remained the standard window material for LCTEM since their use in the first modern LCTEM experiments by Ross and coworkers in the early 2000s (Figure 3B).³³ There are several obvious advantages: chip design and fabrication have become highly advanced; a-Si₃N_x chips can be integrated with inlet-outlet flow lines that allow for external-liquid flow and chemical mixing; a-Si₃N_x windows are physically robust under UHV and are sufficiently low density and thin such that background scattering and noise from the windows are not prohibitive to imaging. a-Si₃N_x window chips are also amenable to the addition of microelectrodes and resistance heating elements, which have enabled in situ electrochemical-(EC)-LCTEM and variable-temperature (VT)-LCTEM. 21,33 However, the assumption that a-Si₃N_x is effectively inert and does not undergo interactions with polymeric solutions breaks down at the nanoscale under e-beam irradiation.82-89

Immediately following fabrication and photoresist removal, the surface of a pristine $a\text{-}\mathrm{Si}_3\mathrm{N}_x$ window will undergo surface reactions with air, water, or other species in the environment, wherein the $\equiv \mathrm{Si}_3\mathrm{N}$ surface is converted to a mixture of hydrophobic and hydrophilic moieties, depending on the specific environment (Figure 4). In ambient air containing moisture in a typical lab environment, the $a\text{-}\mathrm{Si}_3\mathrm{N}_x$ surface will both oxidize and hydrolyze over time, converting exposed surface nitrogens ($\equiv \mathrm{Si}_3\mathrm{N}$) into silylamines ($\equiv \mathrm{Si}\text{-}\mathrm{NH}_2$ or $\equiv \mathrm{Si}_2\text{-}\mathrm{NH}$) and silanols ($\equiv \mathrm{Si}\text{-}\mathrm{OH}$ or $= \mathrm{Si}\text{-}[\mathrm{OH}]_2$), and in high O_2 conditions, forming thin patches of SiO_2 terminated by silanol groups. $^{82,83,86,87,89-94}$ In practice, any real $a\text{-}\mathrm{Si}_3\mathrm{N}_x$

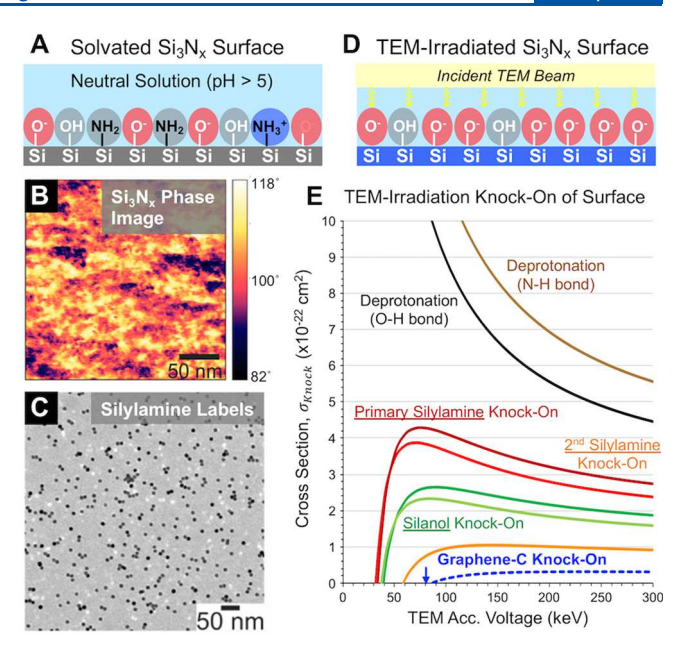


Figure 4. Surface of $\mathrm{Si}_3\mathrm{N}_x$ LCTEM windows. (A) Initial surface chemistry of a solvated pristine $am\text{-}\mathrm{Si}_3\mathrm{N}_x$ window without TEM irradiations (beam off), a mix of silanol and silylamine moieties. (B) In situ liquid chemical force microscopy (CFM) phase image of an air plasma treated $\mathrm{Si}_3\mathrm{N}_x$ window, showing spatial hydrophobic/hydrophilic variations. (C) Dry-TEM image of a $\mathrm{Si}_3\mathrm{N}_x$ window coated with Au NPs labeled to bind to silylamine surface moieties. (D) The net effects of e-beam knock-on of windows during LCTEM; surfaces are more deprotonated (positive surface moieties), and hydrogen bonding is reduced compared to the initial surface without irradiation. (E) Theoretical knock-on scattering cross sections for the various surface species. The prographene-LCTEM, knock-on damage should be prevented below ca. 86 keV (blue arrow). B and C are reproduced with permission from ref 28. Copyright 2019 ACS Publications.

membrane will have a surface chemistry composition that is spatially heterogeneous, with local variations in surface silanol/silylamine content (Figure 4A–C). In liquid, silanols are net deprotonated, yielding a negative charge at neutral pH (pH > ca. 4.5), while silylamines are net protonated, yielding a positive charge at neutral pH (pH < ca. 10). 88,92,93

The zwitterionic nature of untreated a-Si₃N_x surfaces might not be ideal for many polymer systems (Figure 4B,C),²⁸ where one instead would prefer a surface chemistry that is spatially uniform, be it completely positively charged, negatively charged, or neutral. The local and net surface charge chemistry of any a-Si₃N_x window can be tuned by altering the silanol:silylamine surface content, 88 by introducing other surface moieties through chemical window modification (e.g., silanezation)95-97 or by physically coating other materials as films over the a-Si₃N_x surface (e.g., graphene or metal-oxide coatings).⁷⁶ Untreated a-Si₃N_x surfaces are relatively hydrophobic, which is problematic for the assembly of hydrated liquid cells, as poor wetting of the windows often leads to formation of air pockets or dehydrated regions within the liquid-cell vessel. Plasma treatment of windows prior to loading the sample solution can increase window hydrophilicity and will clean the surface of contaminants. This process can also be used to tune the surface chemistry composition, though control is limited. Numerous plasma treatment methods and instruments exist, each affecting the a-Si₃N_x surface differently depending on the conditions and parameters used. For instance, surface atoms can be removed by plasma cleaning

under argon to lower silanol coverage and recover the pristine ≡Si₃N surface. Alternatively, surface atoms can be replaced through exchange processes by plasma cleaning under oxygen to increase silanol coverage. A combination of these two procedures can also be employed using standard RF glow-discharge units with ambient air. 89,98-101 Methods such as photoelectron spectroscopy (XPS) or in situ chemical force microscopy (CFM) can be used to experimentally measure the relative surface concentration of silylamine, silanol, or other surface moieties present and map the spatial distribution of hydrophobic or hydrophilic surface moieties on any LCTEM window (Figure 4B). ^{28,102–106} To date, the use of chemical window treatments to modify the surface of LCTEM windows by forming surface silanes has not been widely explored beyond the chemical surface modifications needed to fix biological specimens. 95–97,107,108 Ultimately, chemical window modification offers the potential for far greater control over the final a-Si₃N_x surface chemistry than is possible using plasma treatments. 89,109,110

■ IRRADIATING THE VESSEL WITH THE IMAGING E-BEAM

1. Effect to the Windows and Interactions at Windows. Acquiring data on a sample within the LCTEM vessel necessitates irradiating the vessel with a keV electron beam. The nature of LCTEM window surfaces and how they interact with and affect the solution drastically changes upon irradiation by the electron beam (Figure 4D). As the incident TEM electrons journey though the liquid-cell vessel, they pass through the top and bottom windows and experience scattering events during their transmission, both elastic and inelastic. Scattering of incident electrons by matter is probabilistic; the mean number of scattering events $(\overline{\#}_{scat})$ that an electron will experience as it passes through a window is directly related to the respective total scattering cross section for the atoms that compose the window (σ, nm^2) , the atom density of the material (N, atom/nm³), and the window thickness (t, nm), $\overline{\#}_{scat} \cong \sigma Nt$. The magnitude of scattering by the windows can be diminished by reducing the window thickness or density or by selecting a window material with a smaller scattering cross section. However, it is important to consider elastic and inelastic scattering separately, as each causes separate artefactual irradiation effects in LCTEM, and each has a separate cross section $(\sigma = \sigma_{El} + \sigma_{In})^{.111,112}$

We label elastic scattering as the scattering interactions that occur between the incident TEM electrons and nuclei of the matter under irradiation. The elastic scattering cross section can be approximated using the Rutherford or Mott cross sections, which both state $\sigma_{\rm El} \propto Z^{4/3}$ to Z^2 depending on beam keV. 10,111,113,114 Any scattering from the windows or any support or substrate effectively acts as an overlaid Gaussian blur on the pure image of the sample, as window scattering will reduce the signal, contrast, and resolution of any image while increasing the background noise, significantly degrading image quality. 70,71 a-Si₃N_x can be considered to have low-background scattering with a relatively small $\sigma_{\rm El}$. Using scattering theory, Li and Knibbe have computed an ca. 1.5 nm loss of resolution due to beam broadening caused by elastic scattering for two 50 nm a-Si₃N_x windows, with potential additional image resolution losses due to the signal-to-noise ratio, which depends on the employed beam flux and the Z-density of the sample, and to inelastic scattering, which depends on the

chromatic aberration of the TEM and can be eliminated using zero-loss energy-filtered TEM, EFTEM. 70,71,115 Overall, this makes a-Si₃N_x a good window material for LCTEM imaging; Al₂O₃ and SiO₂ both have comparable properties. Though a-Si₃N_x is physically robust to the mechanical forces applied by the column UHV, with a Young's modulus of ca. 300 GPa, each window will bow outward, increasing the thickness of the liquid contained between the two windows, with an ca. 0.5 μ m bulging of each 50 nm a-Si₃N_x window that is greatest at the center of each window.⁷¹ Bulging can be minimized and controlled using recent a-Si₃N_x-LCTEM holders with pressure control systems on the inlet/outlet lines and by controlling the window dimensions used. 116,117 By comparison, graphene windows, which are at most 1-2 nm thick and low Z-density, with a Young's modulus of ca. 1000 GPa, are essentially invisible to the beam and thus cause no resolution loss; the best LCTEM resolution and contrast of polymers in liquid can be obtained using monolayer graphene liquid cells, all else being equal.20

However, elastic is an imperfect term to describe all nucleus scattering events, as a small fraction of electrons actually do transfer significant energy to the target nucleus, which can lead to the displacement of that atom, termed knock-on scattering, $\sigma_{\rm El-knock}$ (Figure 4E). ^{118,119} In LCTEM, any knock-on scattering event with an inner-surface atom in the window will result in the ejection of that atom into solution, altering the window surface and generating a solvated and mobile ion in the confined solution (Figure 4D). Knock-on ejection of low-Z surface elements, specifically surface hydrogens, is nontrivial even at low dose rates (large $\sigma_{\text{El-knock}}$ for deprotonation). That is, during LCTEM irradiation, the TEM beam is continually deprotonating surface silanol and silylamine moieties, and this continuous deprotonation achieves equilibrium with competing reprotonation reactions with the solution, as dictated by the solution pH.

Though less frequent compared to surface hydrogens, the irradiating TEM beam will also knock-on eject surface nitrogen and oxygen atoms (silanol and silylamine moieties) at accelerating voltages above ca. 40 keV, 118 an effect which over time will progressively alter the surface composition of the window (Figure 4D,E). Silylamine moieties that are knock-on ejected generally never reform in aqueous solutions; exposed ≡Si⁺ surface terminal groups react rapidly with local water molecules to form stable silanol moieties, while generating solvated H⁺ ions. Over time, LCTEM irradiation leads to a progressive silanolization of a-Si₃N_x windows. This effect is minimized at low beam fluxes. For example, 5 h of continuous irradiation at an electron flux of 1 e-/Å2 s would only result in the degradation of ca. 1/20 of the initial silylamine moieties in the area under irradiation. However, silylamine removal can become significant at high dose rates; at $100 \text{ e}^{-}/\text{Å}^{2} \text{ s}$, ca. one in ten silylamines are removed within the first 5 min of irradiation, using a single scattering approximation. 112,118

Knock-on damage in the case of graphene LC vessels, or other monolayer window materials, is a significant concern, as it can result in the destruction and leakage of the liquid-cell pocket under observation. Based on the binding energy of C atoms in the graphene lattice (ca. 17–22 eV), an irradiating TEM beam can eject C atoms from pristine graphene at accelerating voltages above ca. 86 keV (Figure 4E), 118,120 forming defects that propagate under continued irradiation, which can form large gas bubbles and release the contained solution to the column vacuum, effectively desolvating the

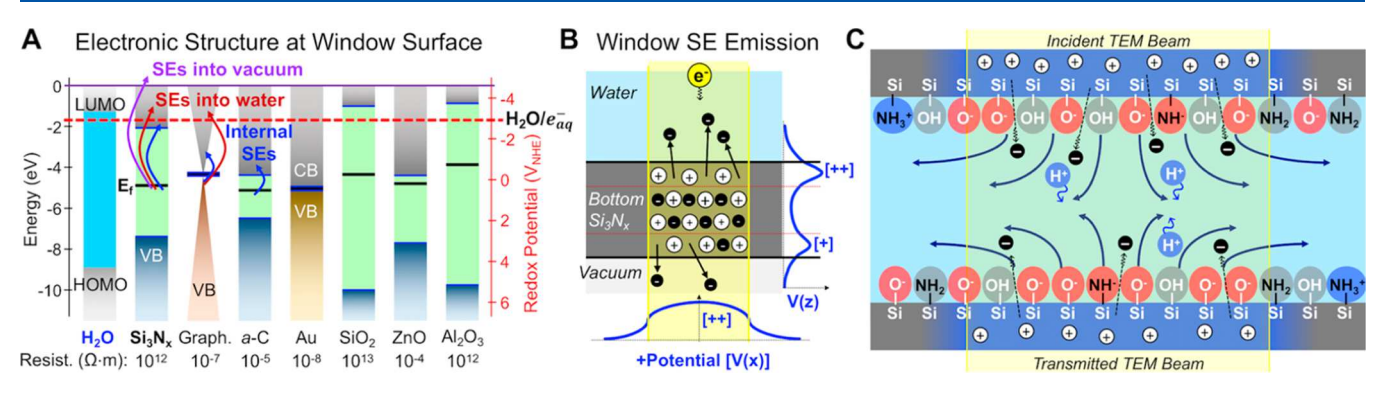


Figure 5. Effects of TEM irradiation on LCTEM windows and the liquid-cell vessel containing the sample solution. (A) Band structure of common/potential LCTEM window materials at the window surface, which dictate the response of the different materials to the TEM beam. Irradiation can induce the emission of SEs into solution if the excited electrons cross the red dashed line (H_2O/e_{aq}^-) . Reproduced with permission from ref 136. Copyright 2014 ACS Publications. (B) Electric potential generation, V(x,z), in an a-Si₃N_x window under TEM irradiation due to ESE emission. More ESEs escape from the solvated side of the window into solution than from the opposite side into vacuum, generating a thickness potential profile, V(z). The TEM beam diameter (vertical yellow beam) defines the full-width, half maxima of the lateral potential profile, V(x). (C) Net effects on the entire liquid-cell vessel as a result of the TEM beam interacting with the a-Si₃N_x windows that include window [+] charging and electric fields, window surface deprotonation, and the release of ESEs and H+ into solution.

sample and ending the LCTEM experiment.^{76,120–122} We note that graphene membranes with defect sites can experience knock-on ejection below 80 keV,¹²² and using windows of multilayer graphene will extend the lifetime of irradiated liquid cells at any keV.^{74,75}

Concurrent with nucleus elastic, $\sigma_{\rm El}$, scattering events, a certain fraction of the incident TEM electrons, are scattered by electrons in the window (inelastic, $\sigma_{\rm In}$), causing the excitation or ionization of molecular atoms or plasmons, the breaking of bonds, and the creation of both internal *excited* electrons and an equivalent number of localized [+] positive charge centers or holes within the window (Figure 5). Fig. 123–126 These excited electrons, termed internal secondary electrons (ISEs), can be subsequently emitted from the window surface into the vacuum or into solution as emitted secondary electrons, ESEs. ESEs are emitted into solution if the electrons are able to reach the membrane surface and overcome the surface barrier, the magnitude of which is defined by the electronic band structures of the membrane material in relation to that of the surrounding medium or vacuum (Figure 5A).

The emission yield of ESEs from the surface of an irradiated window, $\delta = \frac{\# \text{ESEs emitted}}{\# \text{incident electrons}}$, is a function of the TEM beam energy, E_0 ($\delta \propto E_0^{-0.8}$), 127 the probability of ISE generation per incident electron, and the probability of ISE escape from the window surface. The latter two are related to electronic properties of the window, with theoretical and experimental values available for many elements/materials (Stopping Power, ISE escape depth, work function, and electron affinity). $^{127-130}$ Based on Bethe theory and ESE yield measurements at sub-50 keV incident electron beam energies, $^{127,128,130-132}$ the theoretical yield of ESEs emitted into the vacuum from in an a-Si₃N $_x$, or other semiconductor membranes under ca. 50–300 keV irradiation, is on the order of $\delta \sim 0.05-0.25$ ESEs per single incident electron, a value which is independent of membrane thickness for membranes thicker than ca. 10–15 nm, the maximum escape depth of ESEs (Figure 5B). $^{128,132-134}$

For an ISE to be emitted from a solid surface into vacuum, the ISE must be excited above the vacuum level, a significant energy barrier for materials with large work functions (Figure 5A).¹³⁵ However, an ISE with excitation energy below the

vacuum level but above the conduction level, termed a *hot electron*, can be released from the window surface into a solvating liquid if its excitation energy exceeds the redox potential to solvate it in that liquid, $e_{\rm solv}^- = \sim 1.7$ eV, which lies several eV below the vacuum level for many liquids; for water, $e_{\rm solv}^- = \sim 1.7$ eV. ^{136–138} Once hydrated, there will be a larger ESE yield from the interior surface of the LCTEM windows into solution than predicted by theory for emission into vacuum (Figure 5B).

During irradiation, each ESE ejected from the window into vacuum or liquid will leave behind a corresponding hole (Figure 5B), which will persist as a positionally pinned positive charge in low conductivity windows (a-Si₃N_x or oxides) or which will be rapidly neutralized in high conductivity windows (metals or graphene). The ESE yield from each window generates an instantaneous current ($I_{ESE} = I_0 \cdot \delta$, C/s) in the irradiated area, 134 where I_{ESE} is negative and the area of its flow is the cross-sectional area of the irradiating TEM beam, such that the magnitude of the membrane's charging current can be directly reduced by reducing the electron flux, I_0 , or by operating at a higher accelerating voltage. In each window, $I_{\rm ESE}$ generates a potential profile $(V_{\text{mem}}(t,x))$ that varies radially (x)over the irradiated area and changes with irradiation time (t), reaching a steady-state potential, $V_{\text{mem}}(\infty,x)$, where (x) is any radial location within the irradiated area of beam radius, a; r_x is the distance to electrical ground; and d is the window thickness (Figure 5B). 125,133,134,13

$$V_{\text{mem}}(\infty, x) \approx \frac{I_{\text{ESE}}}{4\pi \cdot \gamma_{\text{m}} \cdot d} \left(1 - \frac{x^2}{a^2} + 2 \ln \left[\frac{r_x}{a} \right] \right)$$

Increasing the membrane conductivity $(\gamma_{\rm m})$ (Figure 4A) will directly reduce its steady-state positive potential $(V_{\rm mem}(\infty,x))$, and essentially no charge potential accumulates in a thin, highly conducting membrane (e.g., graphene). However, regardless of material conductivity, all window materials, of equal thickness and at equal keV, will emit roughly similar yields of ESEs into solution, $e_{\rm solv}^-$ (ca. 50 eV), which will alter the solution chemistry and cause additional radiolysis and ionization damage to polymers within the vessel (see next section).

For LCTEM windows that do charge under irradiation (a- $\mathrm{Si}_{3}\mathrm{N}_{x}$), the twin positive potentials $V_{\mathrm{mem}}(\infty,x)$ of the top and bottom windows are separated by an insulating liquid layer, which generates a spatially inhomogeneous electric field within the liquid-cell volume that is dependent on the liquid thickness and the windows' charge potentials and has been modeled by Jiang for different LCTEM vessel geometries (Figure 5C), solutions, and irradiation conditions based on previous charging models for isolated membranes. 133,134,140,141 In brief, window charging generates a positive electric field that is normal to the surface of each window and radially outward from the beam center, 140,141 such that anionic species are driven to the window surfaces and towards the center of the irradiated area, while cationic species are repelled from the surfaces and away from the irradiated area. This charging effect can potentially have a significant influence on the local chemistry and the diffusion of species within the LC vessel.

Coating an insulating window with a thin (ca. 2–5 nm) conducting layer on at least one surface grounded beyond the beam radius can reduce irradiation-induced window charging by altering the electrostatic boundary conditions of the system, reducing the effective distance to ground (r_0) to the order of the membrane thickness. ^{125,133} The maximum reduction in membrane charging will result from coating both interior and exterior surfaces, though coating either the interior or exterior surfaces can potentially have a significant effect on reducing charging during LCTEM irradiation when using a-Si₃N $_x$ windows.

As the LCTEM windows are irradiated by the beam, many inelastic scattering events will not transfer sufficient energy to excite the targeted electron(s) into the conduction band of the material. Instead, these low-energy excited electrons remain in the solid state (Figure 5A), where they experience strong attractive Coulombic interactions with their corresponding hole (Figure 5B), 135 forming solid-state electron-hole pairs with energies below the band gap of the material, termed excitons. In semiconductors, excitons that do not rapidly relax can react with surface hydroxyl or amine groups, causing the breakage of the O-H or N-H bond, deprotonating surface silanol or silylamine moieties, and releasing H⁺ into solution (Figure 5C). 142-144 The deprotonation effect caused by excitons will be complementary and additive to the deprotonation effect caused by elastic knock-on ejection of surface hydrogens, in equilibrium with natural protonation, as dictated by the solution pH.

To summarize (Figure 5C), the irradiating beam induces the emission of ESEs from all window materials into the solution and vacuum, which in turn causes window charging and Efields within the liquid-cell vessel for low conductivity windows $(a-Si_3N_x)$. These ESE effects are reduced at higher keV and lower flux. Simultaneously, the beam will cause window surfaces to become more deprotonated at the steady state and will progressively alter the surface composition over time. Graphene windows can be catastrophically damaged by the beam, which can be minimized by operating at low keV (below ca. 86 keV) and/or using multilayer windows.

2. Direct Effect of the e-Beam on the Solvent. Next, we follow the path of the incident TEM beam into the solution contained in the LC-vessel, where it continues to undergo scattering events, now with solvent molecules and solvated polymers. These scattering events cause solution radiolysis, which alters the solution chemistry and generates species that

can be highly damaging to solvated polymers as indirect beam damage (next section).

In liquids, atoms are not localized within a ridged lattice, and thus knock-on damage by nucleus elastic scattering is generally marginal. However, the electron beam directly damages solution molecules through inelastic scattering events (Figure 6), where the energy transferred by the irradiating beam causes

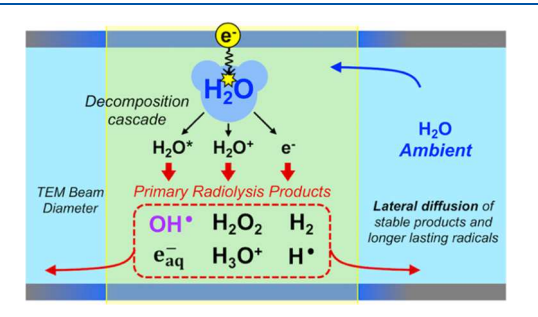


Figure 6. Effect of TEM irradiation on water/solution in LCTEM (radiolysis). Stage 1, the primary scattering event between the incident e-beam and the electron cloud of a water molecule. Stage 2, intermediated states are formed, which decompose though a cascade of reactions, yielding a set of primary radiolysis products at the end of stage 3. Primary products formed under the beam can diffuse away from their sites of formation within the liquid cell; the steady-state primary product concentration is dependent on beam flux, beam diameter/area, liquid-cell thickness, and starting liquid concentration.

molecular deterioration termed as radiolysis. Radiolysis is a multistep process, involving the excitation and ionization of solution molecules, followed by decomposition or thermalization, and a rate-dependent cascade of electrons, radicals, and ions that interact and ultimately yield a set of primary chemical products, specific to the initial radiolytic molecule, that are diffuse in solution. 135,145,146 This multistep process for water is shown simplified in Figure 6. For most liquids, the primary radiolysis products are highly reactive with surrounding solvent molecules or other solvated species, including polymer chains, driving secondary and higher-order chemical reactions, which are discussed in the next section on indirect polymer damage. Numerous LCTEM studies have leveraged the ability to use ebeam-induced water radiolysis to drive chemical or materials processes, most notably to create net reductive or oxidative environments inside of the LC-vessel to induce crystal nucleation and growth and crystal dissolution or to drive monomer polymerization. 50,57,58 However, many chemical and materials processes relevant to polymer chemistry demand the minimization, or ideally the elimination, of any artefactual disturbances to the chemistry of the system by radiolysis or other factors. For LCTEM experiments, we ultimately seek to control and quantify radiolysis chemistry, which requires a fundamental understanding of the radiolysis process of the system under study in the confines of the liquid-cell vessel.

In recent years, the need to better understand solution radiolysis using scattering theory and classical radiation chemistry has been a point of critical concern in the LPTEM field, and we point to several detailed reviews on LPTEM liquid radiolysis theory and the references therein. 139,145–148 Bau, Ross, and coworkers first developed a model using known radiolysis decomposition cascade reactions, inelastic scattering stopping power values, reaction rate constants, and radiolytic yields to calculate the time-dependent and steady-state concentrations of primary radiolysis products in pure water

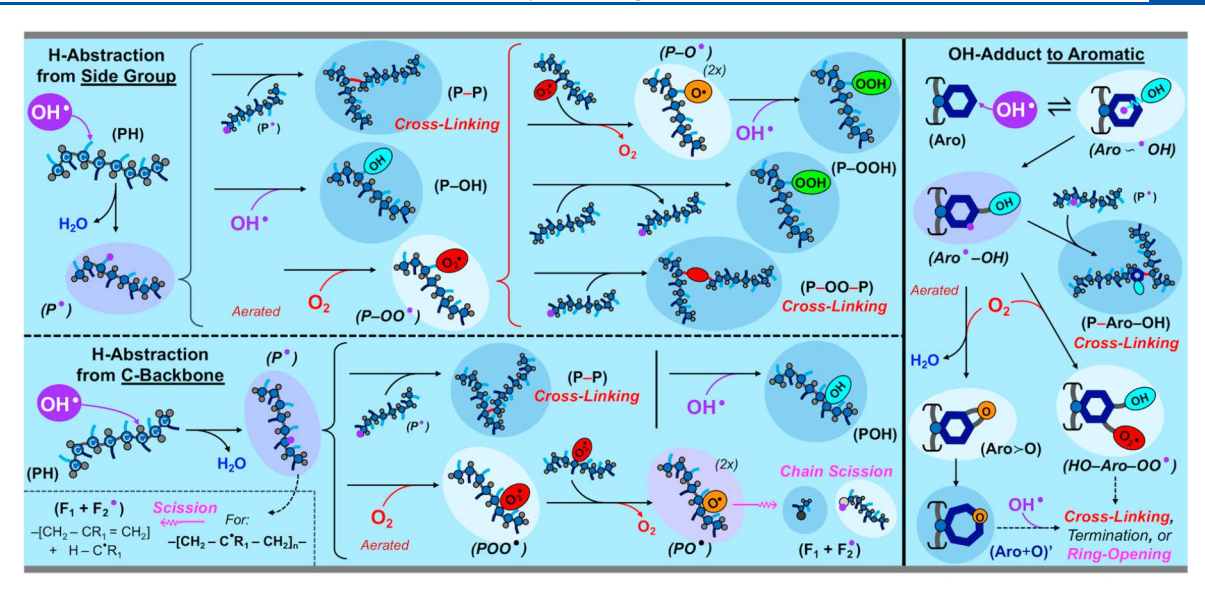


Figure 7. Common chemical [indirect] damage reaction pathways for polymer damage by hydroxyl radicals (solution radiolysis). Damage is initiated by H-abstraction from the polymer by OH[•], forming P[•]. (Top) Polymer damage reactions that follow H-abstraction from a side group and (bottom) from the C backbone. Right: pathways of reaction of OH[•], with an aromatic group that can serve to mitigate indirect damage to aromatic polymers compared to aliphatic polymers. Unstable/intermediate structures are highlighted in white, and stable/product structures are highlighted in blue.

as a function of TEM electron flux. This work allowed for the theoretical determination of aqueous solution chemistry in the irradiated liquid-cell vessel. For water, the primary radiolysis products are OH·, e⁻_{aqt}, H·, H₂, H₂O₂, H₃O⁺, and HO₂·, which each have their own respective yields for a given keV. In radiation chemistry, the yield is customarily denoted as the Gvalue, or the number of molecules created or destroyed per 100 eV of absorbed energy. 135,145-147 The steady-state concentration of a given species in solution is thus a balance between the rate of primary product generation, controlled by the electron flux, solution stopping power (MeV/cm), respective G-values, and the rate of reactions between the primary products and the surrounding solution, intrinsically defined by the rate constants and concentration. 147 We can directly control the steady-state solution chemistry by controlling the electron flux (dose rate)¹⁴⁷ and by controlling the initial solution chemistry and its radiolysis reactions by using chemical additives or scavengers (see below). 148 During TEM irradiation, commercial a-Si₃N_x LCTEM holders with inlet-outlet flow lines (Figure 1A,B) provide some degree of additional control over the in situ solution chemistry in the irradiated region by inducing the diffusion of longer lasting radiolysis products away from the area of irradiation and replenishing this area with nonirradiated solution. 117,149,150 Solution flow can come at the expense of nanomaterial flow or motion, and using liquid flow during in situ LCTEM observation can present a challenge for continuously tracking discrete polymer structures over time.

The Bau and Ross model has recently been expanded to consider the effect of ESEs emitted from the liquid-cell vessel windows or metallic structures into the contained solution; accounting for this effect shows that the local yields of all radiolysis products in solution increase near the $a\text{-}\mathrm{Si}_3\mathrm{N}_x$ window–solution or metal–solution interface, most notably e^- and the oxidants OH· and H⁺. ¹⁵¹ Due to the very low kinetic energy of ESEs released into solution (ca. 50 eV) compared to those of the incident TEM beam (ca. 50–300 keV), ESEs will only travel ca. 10–20 nm (continuous slowing-

down approximation, CSDA, range) in solution before they lose their energy to the solution, causing additional solution radiolysis, and become e⁻_{solv}. That is, each ESE imparts ca. 50 eV energy over ca. 20 nm distance of solution, localized at the window surface. By comparison, the penetration range of 300 keV incident TEM electrons is ca. 85 μ m in water, with a linear stopping power of ca. 2.353 MeV/cm; 153 a 300 keV electron will only impart ca. 5 eV over 20 nm solution, though the 300 keV electron will continue to impart this ca. 5 eV per 20 nm solution throughout its transmission through the entire liquid cell, while ESEs will thermalize over their first 20 nm travelled. 152,153 This window-ESE radiolysis enhancing effect creates a spatially inhomogeneous chemical environment within the irradiated LC-vessel, such that the solution is both radiolyzed and strongly net reducing close to the windows or close to any solvated solid structures. The effect of temperature has also been incorporated into the LCTEM radiolysis model by accounting for the effect of temperature on the G-values and reaction rate constants of radiolytic species. 145,154 Though most nonaqueous solvents have yet to be incorporated into this radiolysis model, G-values and rate constants have been reported for many common solvents, and so it is possible to model the theoretical radiolysis chemistry for many solvents relevant to polymer chemistry. 155 We note that the primary hydroxyl-type radicals formed from the radiolysis of many organic alcohols, for example the hydroxymethyl-radical from methanol radiolysis. 155-157 less reactive with solvated polymers than the hydroxyl radical, 158,159 and indirect damage to polymers in LPTEM should be reduced when solvated in organic solvents compared to pure water. For the same reason, many organic solvents are effective hydroxyl radical scavengers in aqueous solution and can be used as low concentration cosolvents in water to reduce chemical damage to solvated polymers (see next section). To date, there is no method or technique to directly and quantitatively probe the in situ solution chemistry in a liquidcell vessel during LPTEM irradiation, but material probes, such as metal nanoparticles which dissolve or precipitate depending

on the redox chemistry of the liquid-cell environment, can be used qualitatively to assess *in situ* solution chemistry. ¹⁵⁴

Static, single-exposure imaging by LCTEM provides conditions that are less sensitive to radiolysis damage or artefacts compared to continuous videographic observation, as chemical radiolysis damage is kinetically limited and requires time to propagate and accumulate. At very rapid image capture rates and high electron flux, but low total fluence similar to cryo-TEM (sub-10 $e^{-}/Å^{2}$ fluence), it is possible to beat the damage and acquire an accurate single image of a static polymer nanostructure before chemical damage or direct ionization/excitation damage manifests in the physical structure, which is not possible for an LPTEM experiment that involves continuous exposure to produce a video containing many frames over a long period of time. To mitigate direct and chemical radiolysis artefacts to polymers during continuous videography, we must minimize the irradiation flux, operate at higher keV, and employ chemical additives that can prevent or repair damage that does occur. 160

3. Indirect Effects of the e-Beam on Solvated Polymers. Depending on the polymer under study and its unique chemistry and molecular structure, different specific primary radiolytic species will be of concern for causing chemical damage to the solvated polymer chains themselves (indirect beam damage). Based on experimental data from pulsed radiolysis studies of aqueous polymer solutions, there is strong evidence that the hydroxyl radical is largely responsible for polymer damage under ionizing radiation (Figure 7), more than any other radiolytic species and direct irradiation (see next section). 161-167 The hydrated electron, by comparison, generally has a minor damaging effect on polymers (PH \rightarrow PH⁻), but can play a significant role in the chemical radiolysis induced damage of DNA and peptides through strand breakage and could be involved in damage during the LPTEM study of biopolymers. 168

In aqueous polymer solutions, hydroxyl radicals (OH•) have large rate constants for hydrogen abstraction from most polymers $(OH^{\bullet} + PH \rightarrow P^{\bullet} + H_2O)$, which can occur at carbon atoms located along the backbone (Figure 7 top) or in the side groups (Figure 7 bottom), creating highly reactive macroradical polymer chains (P•) within the irradiated volume. For carbon atoms located in aromatic groups, however, the rate of H-abstraction by hydroxyl radicals is suppressed compared to aliphatic carbons, and instead a pathway leading to a hydroxy adduct is predominant at ambient temperatures (ca. 19:1 OH-adduct formation to Habstraction) (shown in Figure 7 right). The formation of the OH-adduct in aromatics begins with the formation of a metastable pre-reaction complex, where the hydroxyl radical is loosely bound through electrostatic interactions. Depending on the specific structure of the aromatic ring, the metastable complex can rearrange into one of several aromatic adducts in the form of hydroxy-aromatic macroradicals.¹⁷¹ For many aromatic structures, the energy barrier for rearrangement of pre-reaction complexes into adducts (Aro*-OH) is larger than for OH dissociation, and aromatic units effectively scavenge a fraction of the hydroxyl radicals in solution without experiencing any molecular alteration or damage. 172

In a deaerated solution, polymer macroradicals, including hydroxy-aromatic macroradicals, that *meet* will form covalent bonds ($P^{\bullet} + P^{\bullet} \rightarrow P - P$), cross-linking or gelling the polymer sample, which can significantly alter the physical and chemical properties of the polymer, beyond just increasing molecular

weight. Weight. The cross-linking kinetics are affected by the location of hydrogen abstraction sites in the polymer, steric constraints specific to the polymer, and competition with other P^{\bullet} radical-termination reactions. For example, P^{\bullet} can react with a second hydroxyl radical to form stabilized [terminated] but altered P-OH, or it can react with a local hydrogen radical to self-heal ($P^{\bullet} + H^{\bullet} \rightarrow PH$).

Cross-linking reactions between polymer macroradicals can occur after H-abstraction from any location on the polymers, though cross-linking is less sterically hindered, and thus more rapid and probable, for carbon radicals in side groups than in the backbone. Certain polymers, particularly those of the form [-CH₂-CRH-CH₂-] can also readily undergo scission when radicalized by H-abstraction from C atoms in the polymer backbone from the nonmethylene carbon, resulting in formation of lower molecular weight fragments (Figure 7 bottom left). H-abstraction from side groups cannot generally lead to backbone scission, and the lack of protonated carbons in the backbone of a polymer will help to protect against backbone scission, resulting from hydroxyl damage, though fragmentation of side groups can still occur. In fully deaerated solutions, scission due to hydroxyl radical Habstraction should be very minor in most polymers (except for the class of polymers discussed above), and polymer damage will primarily take the form of cross-linking or minor molecular modification.¹⁷

In aerated aqueous solutions (Figure 7), polymer macroradicals readily react with O_2 to form peroxyl $(P^{\bullet} + O_2 \rightarrow$ PO_2^{\bullet}) radicals and highly unstable oxyl radicals $(PO_2^{\bullet} + PO_2^{\bullet} \rightarrow$ PO + O₂), which can self-decompose into fragments through chain scission $(PO^{\bullet} \to F_1 + F_2^{\bullet})$ at the location of the oxyl radical. Backbone scission by this mechanism requires the formation of an oxyl radical directly in the backbone, and polymers dense with methylene or (-CRH-) units in the backbone tend to be especially prone to scission in aerated solutions. 175-179 The hydroxy-aromatic macroradical can also react with O2 to form an aromatic oxide, instead of a peroxyl radical, and ultimately an aromatic oxepin, which can undergo ring opening with reaction with a second OH[•], ¹⁷¹ providing aromatic polymers additional OH scavenging ability over aliphatic polymers (Figure 7 right). Note, an individual polymer chain can undergo the two-peroxyl to single-oxyl radical reaction with itself, for example, the collision between a peroxyl radical in a side group and one adjacent in the backbone, which allows polymer scission to occur in high oxygen concentration solutions even at low polymer concentrations. Radicalized polymer chains can also cross0link in aerated solutions through an [-OO-] bridge prone to subsequent scission (see below) (Figure 6). 174

The relative magnitude of cross-linking versus chain scission will depend on the polymer and O_2 concentration, the presence of other additives, the structure of the polymer, and the electron flux; together, these factors control the kinetics of scission versus cross-linking reactions and the steady-state concentration of hydroxyl radicals and thus the steady-state concentration of P^{\bullet} . Increasing the polymer concentration or the OH^{\bullet} scavenger concentration will decrease the damage from hydroxyl radicals to each individual polymer chain, while also altering the rates of cross-linking and scission. As a general rule, deaerating aqueous polymer solutions should reduce hydroxyl-induced backbone scission, though it will have little effect on cross-linking, which can be reduced by lowering the polymer concentration or increasing the scavenger

concentration (see next section). We note that cross-linking is an artefact that can be hard to detect *in situ*, as cross-linking might not cause detectable changes to a polymer structure's physical morphology or size. However, cross-linking can have a large effect in altering the physical-chemical behavior of polymer chains and assemblies and must be avoided for LPTEM experiments seeking continuous videographic observation of dynamics or processes.

Intelligent polymer design can be used to create polymer samples that will experience less damage during LCTEM irradiation. If one is unable to modify the sample chemistry or the polymer structure, simply reducing the electron flux will directly reduce hydroxyl radical induced beam damage. However, a nonzero flux is required to image or video a sample in LCTEM, and damage due to solution radiolysis cannot be eliminated entirely by controlling imaging conditions. Adding certain species that readily scavenge or eliminate hydroxyl radicals, such as alcohols or thiol-based small molecules, by converting them into less reactive, unreactive, or terminated species, can provide a means to reduce or possibly eliminate indirect, hydroxyl radical-induced beam damage to polymers in LCTEM (Figure 7).

■ ADDITIVES TO PROTECT OR REPAIR POLYMERS FROM OH* DAMAGE

Presently, the use of additives has been a largely unexplored means to reduce polymer damage in LCTEM. Control over electron flux has been primarily used, and there have only been several examples of using organic alcohols or small molecules as hydroxyl radical scavengers in LCTEM. 31,148,160,180,181 The compatibility and efficacy of different additives as hydroxyl radical scavengers are highly sample dependent, and there are numerous potential scavengers to explore, including antioxidants, such as vitamin E. 174 From decades of fundamental radiation chemistry studies, there is a strong body of literature on hydroxyl radical scavengers, with experimental data on scavenging efficacy for a variety of soft matter systems. Broadly, we can classify hydroxyl radical scavengers into three primary classes of differing effect (Figure 8 top): (1) those that convert the OH radical into a less reactive radical that is less damaging to polymers (i.e., alcohols or uric acid), 159 (2) those that terminate the OH radical while generating ions that alter the solution chemistry (i.e., KI or KBr), 182 and (3) those that terminate OH adicals with no radical byproducts by converting OH to a terminated species (i.e., alkenes or thiourea). Generally, additives in the third class make the ideal scavengers assuming equivalent scavenging rate and efficiency, as the chemistry of the solution will be least affected by their scavenging of OH (fully terminated). Graphene, either as nanosheets in solution or as a window material, also falls into this third class of scavengers (hydroxyl sponge), a significant added benefit of graphene-LCTEM or graphene coatings on a-Si₂N_x windows. ^{76,160} The second class can have detrimental effects in LCTEM, as the ions released can readily form solid precipitates or be incorporated into polymer chains or macromolecular assemblies. 61,62 The first class is broadly compatible across aqueous and organic polymeric solutions, and the radicals formed for many alcohols are comparatively inert towards polymer damage compared to un-scavenged hydroxyl radicals. ^{20,148,160}

Beyond the use of additives to scavenge radiolysis species before they can react with and abstract H from polymer chains, there is also a class of additives that can be considered

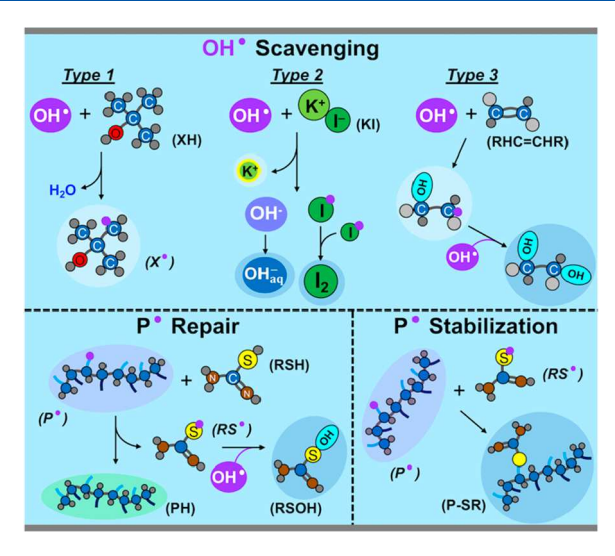


Figure 8. Chemical means to mitigate indirect/chemical and direct beam damage to polymers in LPTEM (solution additives). (Top) Three types of hydroxyl radical scavenging additives. (Bottom) Sulfur containing additives that can repair (left) or stabilized damaged (radicalized) polymers.

"polymer healers" (Figure 8 bottom), which can directly repair radicalized polymer chains by hydrogen transfer to the polymer (left) or can directly stabilize radicalized polymer chains by bonding to it and terminating radicals from the polymer while slightly altering the molecule (right). 183,184 Many sulfur-based compounds, including colloidal sulfur, glutathione, thiourea, and cysteamine, have the ability to both chemically repair and stabilize radicalized polymers 183,184 and should be explored for their efficacy to mitigate or even heal polymer damage in LCTEM. As a final point, the radiolysis G-values of deuterated water are reduced compared to those of nondeuterated water under equivalent TEM irradiation conditions. 160 Using a deuterated solution is akin to the addition of a mild radical scavenger that does not alter solution chemistry and can provide some mitigation of indirect beam damage to polymer samples in LCTEM. 43,55,160

4. Direct Effect of the e-Beam to Solvated Polymers. In addition to the indirect, or solution radiolysis based, damage to polymers that occurs during low linear energy transfer (LET) ionizing radiation of polymer solutions, such as keV TEM electrons, 161-167,185 direct irradiation damage to polymers is also operative during LCTEM and can be significant for high polymer concentrations or high scavenger concentrations, and must be considered as well to understand the true chemistry within the liquid-cell reaction vessel (Figure 9). 179,186-188 The process of polymer molecule radiolysis occurs though a sequence of events, 189,190 broken down into three initial temporal stages: stage 1, (physical) the primary scattering event where energy (ΔE) is transferred to the polymer's electron(s) by the incident TEM radiation, exciting and possibly ionizing the polymer, 135 stage 2 (physico-chemical) where the energy is dissipated by dissociative relaxation, autoionization, thermalization, and/or transfer, starting the formation of primary radiolysis products, and stage 3, (chemical) where localized radicalized polymer-polymer and polymer-solution reactions occur and damage further propagates by molecular rearrangement, scission or fragmentation, and crosslinking or gelling. 135,191 For many polymers, the radical polymer cation intermediate states formed in stages 1 or

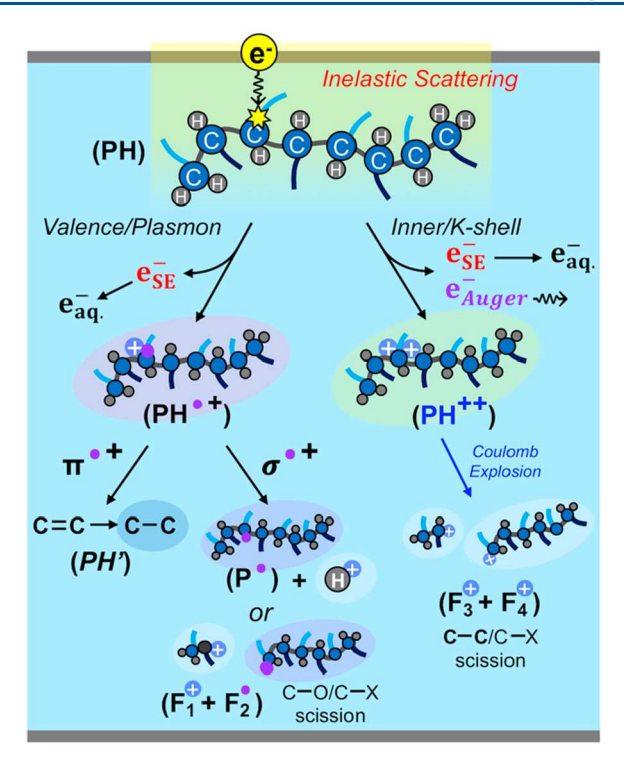


Figure 9. Generalized pathways of direct damage to polymer by TEM beam irradiation (inelastic scattering). Ionization of valence- π electron generally leads to minimal damage in the form of slight molecular arrangement and release of e_{SE}^- . Ionization of valence- σ electrons generally leads to deprotonation or scission of non-[C-C] bonds (e.g., deprotonation) in the chain (and release of of e_{SE}^-). Ionization of inner (K) shell electrons creates double-ionized carbon atoms that can scission the chain by Coulomb explosion (and release of of $e_{\text{SE}}^- + e_{\text{Auger}}^-$).

2 are very similar to those formed via hydroxyl-radical induced chemical damage, and stage 3 of polymer radiolysis can involve many of the same damage propagation reactions as those shown in Figure 7, which result following the deprotonation of the polymer and which can be influenced by different chemical additives, as discussed above. ^{173,192}

In electron microscopy, the convention is to define the "electron irradiation dose" as the total fluence delivered to the sample in units of number of incident e^- per area, $e^-/\text{Å}^2$, or as the fluence rate (aka flux) $e^-/\text{Å}^2$ s, ¹⁸⁹ which are independent of

the sample. However, the *effective total radiation dose* experienced by any molecule in the sample is dependent on the fraction of the incident fluence that is transferred to that molecule during irradiation, given by its mass collision stopping power $(s_{\rho} = -\frac{dE}{\rho \cdot dx})$, MeV cm²/g). ^{111,118,185,189,190}

For an equal mass, a polymer chain with a lower s_ρ will absorb less energy for an equivalent beam fluence (e^-/\mathring{A}^2) and will effectively experience a lower irradiation dose for the same TEM conditions. $^{111,193-195}$

$$s_{\rho} = \left[\frac{N_{\rm A} \cdot Z}{A}\right] \cdot \int \Delta E \left(\frac{d\sigma_{\rm Inel}}{d\Delta E}\right) d\Delta E \approx \left[\frac{N_{\rm A} \cdot Z^*}{A}\right] \cdot \overline{\Delta E} \cdot \overline{\sigma}_{\rm Inel}$$

It is important to note that the numeric amount of total energy absorbed (s_{ρ}) in stage 1 is not necessarily reflective of ultimate polymer damage at the end of stage 3. That is, the way(s) in which the polymer handles the absorbed energy in stages 2 and 3 plays an equally significant role in its damage. The average total energy absorbed by a molecule is comprised of a set of most frequent specific excitations and ionizations, ¹⁸⁵ which can be empirically measured using electron energy loss spectroscopy (EELS). ¹¹¹ An EELS spectrum experimentally quantifies the types (ΔE) and frequencies ($\sigma_{\rm Inel}$) of polymer ionizations and excitations that occur from direct e-beam irradiation in the dry state, which is shown for several polymers, solvents, and organic molecules in Figure 10. ^{179,186,187}

The energy transferred (ΔE) from each inelastic scattering event with a polymer promotes the *struck* electron(s) to excited states above the HOMO level: 176,185,192,196,197

$$(PH + \Delta E) \rightsquigarrow PH^*$$

If the excitation has sufficient energy (ΔE) to promote the target electron above the vacuum level, it will be emitted from the polymer as a secondary electron, creating a polymer radical cation $(PH^{\bullet+})$. ^{185,192,196,197}

$$PH^* \Rightarrow PH^+ + e_{SE}^-$$
 (ionization – valence)

When an inner-shell (K, L, M, etc.) electron is ionized, the down-cascade filling of the deep-level hole gives rise to Auger electron emission, ¹⁸⁶ leading to double (or higher) ionization of the molecular atom, which can rapidly decompose though Coulomb explosion. ¹⁹⁷

$$PH^* \Rightarrow PH^{++} + e_{SE}^- + e_{Auger}^-$$
 (ionization – valence)

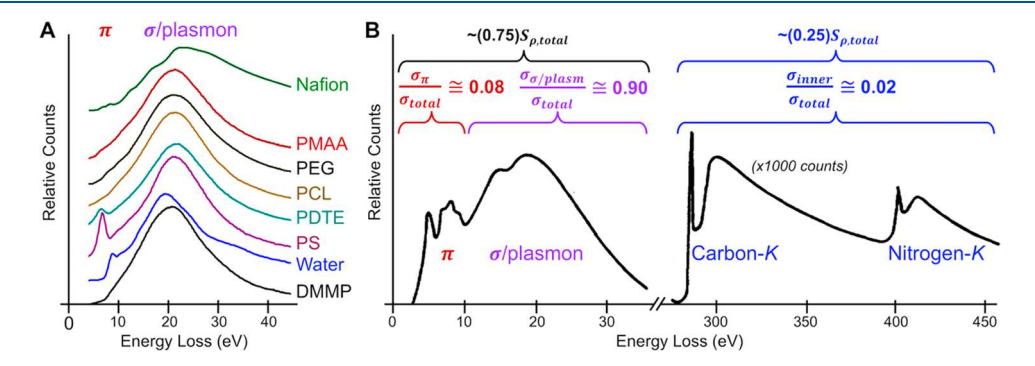


Figure 10. TEM EELS spectra of organic molecules and polymers. (A) Low-loss spectra (valence excitations/ionizations) of various dry polymers and cryo-vitrified solvents. Note the large π -peaks in PS and PDTE, the only aromatic polymers. Reproduced with permission from ref 208. Copyright 2008 Elsevier. (B) Low-loss and core-loss spectra of dried nucleic acid base adenine (dried film on carbon film), with relative contributions of the different excitation peaks to the total energy absorbed (S_p) and the relative scattering cross sections (frequencies) ($\sigma_{\pi p}$) of the different excitation peaks indicated. Reproduced with permission from ref 198. Copyright 1973 Allen Press.

The energy transfer, ΔE , needed to ionize or excite inner-shell electrons (for example $C_{\rm K} \sim 284$ eV) is far greater than to excite or ionize valence electrons (~5-30 eV), and thus the probability for inelastic scattering $(\frac{d\sigma_{Inel}}{d\cdot E})$ and the total amount of energy transferred during inelastic scattering (s_{ρ}) is much larger for valence electrons than for inner shell electrons (Figure 10B). 193–195,198 In amorphous carbon, a decent representation of a generic polymer carbon backbone, valence and plasmon excitations, and ionizations are two orders of magnitude more frequent than K-shell ionizations based on theory and experimental measurements, with ca. 100 valence ionizations per 1 K shell ionization. 186 Reducing molecule damage that occurs as a result of valence electron excitations or ionizations has the most potential to significantly reduce overall direct damage to a polymer sample; damage from Kshell ionization is very difficult to avoid or mitigate for all organic molecules.

In stage 2, the various ionizations and excitations formed in the polymer in stage 1 have time to relax, which can occur via several different pathways of differing molecular effect, 176,185,192,199 through energy transfer processes to the immediate surroundings as *non-damaging de-excitation*: 176

PH*
$$\rightarrow$$
 PH + heat, PH* + $X_{\text{solv}} \rightarrow$ PH + X_{solv}^* or PH* + $H_2O \rightarrow$ PH + H_2O^*

or through self-relaxation as *mildly damaging de-excitations* through bonding or molecular rearrangement: ¹⁹⁹

$$PH^*_{(C=C)} \rightarrow PH'_{(C-C)}$$

While ionized polymers can relax through electron transfer processes from the surroundings to the polymer as non-damaging deionization: 176,199

$$PH^+ + X_{solv} \rightarrow PH + X_{solv}^+ \text{ or } PH^+ + e_{aq}^- \rightarrow PH$$

or through a self-dissociative scission or deprotonation process as *damaging de-excitation/deionization*: ^{176,196,197,199,200}

$$\begin{split} PH^*/PH^{**} &\rightarrow P^{\cdot} + H^{\cdot} \text{ or } PH^*/PH^{**} \rightarrow F_{A}^{\cdot} + F_{B}^{\cdot} \\ PH^{+} &\rightarrow P^{\cdot} + H^{+} \\ &\text{ (or } PH^{+} \rightarrow F_{C}^{\cdot} + F_{D}^{+}, \text{ no } C - C \text{ scission)} \\ PH^{++} &\rightarrow F_{F}^{+} + F_{F}^{+} \text{ (Coulomb explosion)} \end{split}$$

A primary ionization event, yielding energized e_{SE} and e_{Auger} in solution, can go on to propagate additional secondary (and higher-order) ionization or excitation events, effectively self-catalyzing polymer damage and local solution radiolysis. In addition to primary beam damage, there is evidence that ebeam damage to valence and bonding electrons in polymers is at least partly due to the e_{SE}^{-}/e_{Auger}^{-} that are emitted from innershell (K-shell) ionizations.

USING EELS SPECTROSCOPY TO UNDERSTAND DIRECT BEAM DAMAGE TO POLYMER SAMPLES (COMPLEMENTARY PRE-LPTEM ANALYSIS)

There are no techniques for quantitative chemical or molecular-structure analysis that can be applied in real time during an *in situ* LCTEM experiment. That is, we are unable to accurately track molecular changes to either the solution or the polymers *in situ* with current instrumentation. Therefore, *post*

mortem verification of structure and chemistry is critical (see next section). Though many TEMs used for LPTEM videography are equipped with both X-ray and electron energy loss spectrometers (EELS), the background noise that is generated from the thick liquid layer and windows washes out any features related to the solvated polymers of interest, and in situ LCTEM spectroscopy of polymers is of most utility for measuring the approximate liquid thickness in the LC-vessel or for qualitative mapping of high-Z species. 62,116,202,203 However, prior to running an *in situ* LCTEM experiment, we can run EELS analysis of a dried film (thin section)^{179,201,204–207} of our polymer sample to probe the various ionizations and excitations that comprise the total energy absorbed by that polymer during TEM beam irradiation at specific flux, fluence, and keV conditions. Such an analysis would yield information into direct beam damage to the polymer relevant to LPTEM. That is, we can use dry-TEM EELS of our polymer structures to identify peaks that correspond to groups within the polymer structure that will be potentially susceptible to beam damage in situ, such as disulfide bonds. This information can be used to either design more robust polymers for LCTEM or to select specific chemical additives that can repair or reduce some specific form of molecular damage identified by EELS.

For organic molecules or polymers under TEM beam irradiation, scattering events with $\Delta E \leq 10$ eV correspond to excitations in the UV absorption spectrum, those related to valence- π excitations $(\pi \to \pi^*)$ and valence- π ionizations $(\pi \to \pi^{\bullet+} + e_{SE}^-)$ (Figure 10). 186,188,198,204,206,208,209 These low-energy excitations are described by the material's dielectric function, 178,206,210 and DFT methods can be used to model valence level excitations. ¹⁷⁸ Due to the very low ΔE involved and the delocalized nature of π -bonding electrons in carbon molecules, the energy transferred in $(\pi \to \pi^*)$ excitation events is also delocalized²¹¹ and generally does not lead to complete bond breakage in the polymer; the excited state is distributed over several C atoms and relaxes via non-damaging deexcitation, PH* \rightarrow PH). ^{201,209} The ionization of π -bonded electrons, $\pi \rightarrow \pi^{\bullet+}$ + e_{SE}^- , results in the instantaneous alteration to the polymer's bonding structure (C=C \rightarrow C-C^{\bullet +}); the double bond converts to a radical-ion single bond (Figure 9), and complete C-C bond scission is generally avoided by a slight molecular rearrangement or by intrapolymer electron transport in conductive polymers. 188,212,213 Aromatic compounds and polymers containing phenyl groups have especially large peaks in the $\pi \to \pi^*$ excitation region, reflective of the high density of C=C π -bonds, ^{209,210,214,215} and are generally more resistant to direct radiation damage in bulk polymer samples.²¹⁶

In polymers, the next ubiquitous excitation peak in the EELS spectrum corresponds to single-electron $\sigma \to \sigma^*$ excitations and plasmon $(\pi + \sigma) \to (\pi + \sigma)^*$ excitations, which have ΔE in the range of ca. 15–40 eV and comprise the majority of the energy absorbed from the incident irradiation depending on the density of double bonds in the structure (Figure 10). Phase bonded valence electrons are comparatively localized, and their excitation to an antibonding (σ^*) state is not dissipated as readily and leads to an unstable, antibonding state located at the targeted $\sigma^*(C-C)$, $\sigma^*(C-H)$, or $\sigma^*(C-X)$ bond. Though the C-C bond is energetically weaker than the C-H bond, the $\sigma^*(C-C)$ excitation is able to move along a continuous polymer carbon backbone or side group away from its site of initiation, and C-C bonds in the backbone are relatively stable following excitation, the exception being

quaternary carbons. ^217,218 The C–H bond, by comparison, is highly susceptible to scission following excitation to $\sigma^*(C-H)$, either through its direct primary excitation or through excitation transfer from an adjacent $\sigma^*(C-C)$ in the polymer, and σ^* excitations and ionizations will predominately lead to polymer deprotonation PH*+/PH* \rightarrow P* + H*-//H* (Figure 9), similar to the effect of reaction with a hydroxyl radical (Figure 7); 176,200,219 however, it can also result in the breakage of other C–X bonds that might interrupt the continuous carbon backbone. $^{178,212,220-222}$

Lying at far higher ΔE are the family of peaks for the lowfrequency inner-electron excitations and ionizations, specifically the carbon-K edge at ca. 284 eV (Figure 10B). 179,186,210 K-shell ionizations result in multiionization and Auger electron emission, creating highly unstable molecular carbon cations, C++, that can rapidly self-decompose though Coulomb explosion and fragmentation. 197 That is, inner shell excitations and ionizations can cause chain scission at the target atom, regardless of structure, and cannot be mitigated significantly through polymer design. K-shell ionization also yields $e_{\rm SE}^-$ and e-Auger, which cause additional local radiolysis damage to adjacent polymer and solvent molecules. 201 Reducing the fluence or increasing the beam accelerating voltage is the only effective means to reduce damage from inner shell ionizations and excitations, and once formed, these excitations cannot be readily dissipated without creating significant molecular damage. Valence excitations by comparison can be healed or scavenged to some degree by chemical additives or through polymer structure design.

For damage that causes changes to the polymer's electronic bonding structure, EELS can not only be used to determine the relative frequencies of the different primary (stage 1) excitations and ionizations but also be used to track how the primary damage propagates in the polymer over time or with increasing applied fluence. $^{187,198,205-207}$ Any excitation or ionization peaks in the EELS spectrum that significantly change in intensity and shape with increasing irradiation time (fluence) correspond to weak points in the molecule, ²⁰⁶ that is, the types of irradiation-induced excitations that cause damage to the polymer that could be potentially addressed though polymer design. 186,187,206 For example, TEM irradiation of saturated polymers causes C-H bonds to break, and as a result, C=C bonds can form in the polymer, which will be reflected in the appearance of a $\pi \to \pi^*$ peak at ca. 5–7 eV and in some samples a trapped H_2 gas peak at ca. 13 eV. ^{207,220} The plasmon $(\pi + \sigma) \rightarrow (\pi + \sigma)^*$ peak at ca. 20–25 eV also generally blue shifts to higher eV during polymer irradiation, indicating the loss of density of states (DOS) in the polymer caused by broken C-H (or C-X) bonds. 178,204 Highly aromatic polymers, by comparison, will generally express a decrease in the $\pi \to \pi^*$ peak at ca. 5–7 over irradiation time, reflecting the molecular rearrangement (C=C \rightarrow C-C^{\bullet +}) that serves to mitigate gross molecular damage via scission or deprotonation. 204,206 Comparing several polymers of different structures using EELS, all containing C=C bonds or aromatic rings, Singh et al. have found that the "critical does", defined as the cumulative fluence (C/m²) required to reduce the $\pi \to \pi^*$ EELS peak to (1/e) of its original, undamaged intensity, can vary between polymers by several orders of magnitude, suggesting that the specific polymer structure does play a major role in its sensitivity to direct TEM beam damage.² For example, the critical doses required for polycarbonate (PC) or poly(methyl methacrylate) (PMMA) damage are ca.

 $100\times$ less than those required for polystyrene (PS) or styrene maleic anhydride (SMA) damage, with polyethylene terephthalate (PET) falling somewhere between. That is, PS and SMA are far less sensitive to direct TEM damage than the other polymers tested and would make more ideal candidate samples for LCTEM studies.

For polymers that have oxygen atoms interrupting continuous carbon backbones, the C-O bond is sensitive to scission, and these types of polymers tend to be prone to damage via scission and fragmentation. ²²⁰ Esters, carbonates, and -SO₂- are especially susceptible to scission. 178,212,221,22 The presence of O₂ gas in solution can cause oxyl radicals to form in continuous C-backbones following deprotonation, and these oxyl radicals are highly susceptible to scission; for most polymers, scission is minimized by deaerating solutions (Figure 7). 223 The addition of an aromatic ring next to carbonyls or other scission-prone bonds also helps stabilize the polymer against chain scission. ^{178,205} In deaerated conditions, continuous carbon backbones that take the form of $[-CH_2-C^{\bullet}R-$ CH₂-] are prone to scission by the mechanism in Figure 7 (bottom left), $^{175-179,224,225}$ though cross-linking will also occur in kinetic competition with scission in these polymers following deprotonation. Fluorinated versions of polymers tend to be more susceptible to scission, as fluorine atoms provide extra steric hindrance and large Coulombic repulsion, which prevents cross-linking and preferentially promotes the scission of C-C bonds. 216,226 Generally, increasing the size or density of side groups in the polymer will increase the relative proportion of crosslinking versus scission damage.

Aromatic polymers, with rings either in the backbone or in side groups, tend to be far less irradiation sensitive than aliphatic polymers. In aromatics, damage requires larger applied fluence and tends to take the form of cross-linking or minor molecular rearrangement instead of backbone scission. 156,175,215,222 The π -conjugation structure is able to dissipate some amount of the absorbed energy without molecular damage. 178,201,206,212,216 When aromatic groups are incorporated into the polymer structure, the polymer is able to dissipate a larger fraction of absorbed energy though nondamaging means than aliphatic structures, reducing the amount of direct damage experience for a given TEM fluence. 215 Furthermore, aromatic groups not in the polymer itself but as additives in solution can also serve as energy sponges for excited polymers to transfer their excitation energy without causing damage to the polymer itself (PH* + Arom \rightarrow PH + Arom* \rightarrow Arom + ΔE). That is, aromatic alcohols or aromatic versions of other additives have the potential to both scavenge hydroxyl radicals and de-excite excited polymers.

5. Post Mortem Analysis: Validation of Chemistry after in Situ LPTEM. As we have described in detail above, polymer solutions during LPTEM are highly sensitive to the electron beam, which can cause significant molecular damage or other alterations to polymer chains and assemblies as well as to basic chemical reactions and processes. In situ observation of polymers or any material is potentially influenced by these damage artefacts, the magnitude and nature of which must be understood to fully interpret the obtained LPTEM data. Hence, correlative imaging and post-LPTEM post mortem analysis are key to corroborate and contextualize LPTEM findings, especially when videoing dynamic chemical or physical processes, such as morphological conformations, phase transitions, or material formation in situ.

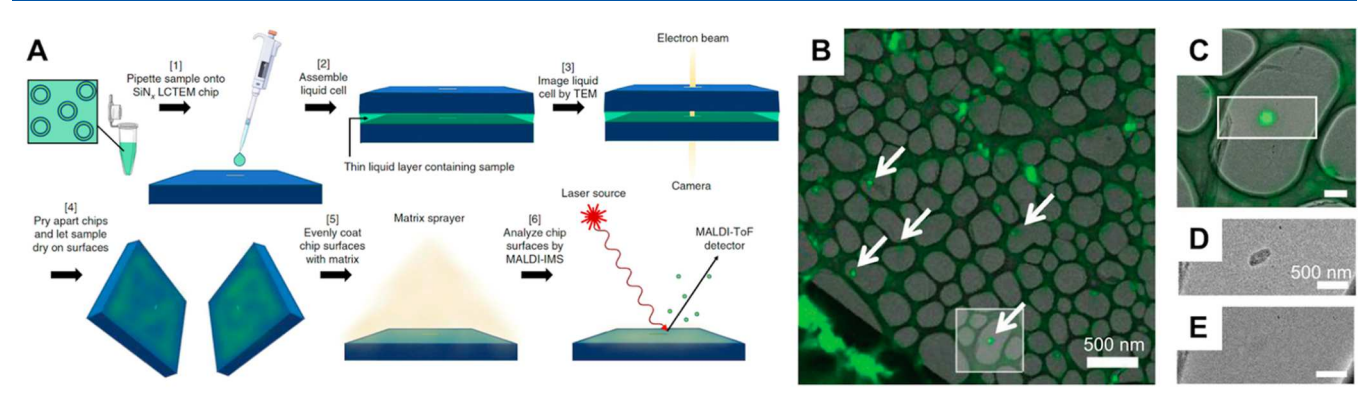


Figure 11. Overview of the MALDI-IMS *post mortem* analysis. Reproduced with permission from ref 49. Copyright 2019 Springer Nature. (B) Correlated fluorescence liquid-phase electron microscopy. (C) Overlay of a fluorescent image and a high-magnification electron image of the white square in B, showing an isolated graphene liquid cell pocket. (D) LPTEM image of the area indicated by the white square in (C) showing the darker contrast of a liquid cell. (E) The liquid cell in D after exposure to the focused electron beam during LPTEM, confirming that the feature was liquid and has been degraded by irradiation. B—E are reproduced with permission from ref 78. Copyright 2020 Wiley-VCH.

LPTEM post mortem is most commonly performed by prying open the used Si₃N_x chips, and then conducting drystate TEM characterization of the dried material that remains adhered to the windows. In this way, crystalline phases and materials can be easily analyzed by traditional TEM techniques, specifically electron diffraction, lattice-resolution high resolution (HR) TEM imaging, energy dispersive X-ray spectroscopy (EDS), and EELS; using these techniques, precise crystalline structures can be identified to confirm the growth of a specific phase or structure during the in situ LPTEM experiment. 22,47,58,227,228 This has proven effective for post mortem analysis of protein crystals, biomolecule crystals, and covalent organic framework crystals grown during LPTEM experiments. 58,228,229 However, polymeric systems are generally amorphous or semicrystalline and cannot be analyzed in the same fashion as crystalline materials to verify their structure. For example, a polymer nanoassembly that has solely cross-linked due to in situ LPTEM will have little to no change in its EDS or EELS spectra if its elemental composition is unchanged, and the post mortem acquisition of either EELS or EDS will cause additional damage to the sample, complicating the results (damage due to LPTEM vs due to post mortem EDS/EELS). For post mortem of noncrystalline polymers, analytical sensitivity to chain molecular weight or to specific chemical probes is critical.

Touve et al. developed a post mortem spectrometric method to analyze the molecular weight fragments of peptides following LPTEM (Figure 11A) using high spatial resolution matrix-assisted laser deposition/ionization imaging mass spectrometry (MALDI-IMS) applied to the used, separated LCTEM chips. 49 Other non-TEM spectroscopy techniques, like X-ray photoelectron spectroscopy (XPS), have shown potential for the analysis of soft materials. XPS was applied to probe the adsorption of metal ions to liposomes and evaluate the oxidation state of the metal ions following electron beam irradiation.⁶² In graphene liquid cells, fluorescent labelling can be used to locate imaged features (Figure 11B-E). With the fluorescent tag, the whole grid can be screened using light or fluorescence microscopy, allowing us to detect the exact location of a fluorescent tagged specimen in the TEM grid. This correlative fluorescence microscopy and LPTEM method enables data collection with limited electron beam exposure to the sample, minimizing radiolysis induced chemistry. Further development of novel post mortem methods is still needed, especially techniques with the ability to identify different forms of molecular damage to polymer chains beyond gross changes in chain molecular weight.

6. LPTEM Imaging and Videography Modalities. A common theme through all the sections above is the need to irradiate polymer samples during LPTEM at (A) the lowest possible flux $(e^{-}/Å^{2}\cdot s)$ to minimize both the steady-state concentration of radiolysis species and the magnitude of beamwindow effects (e.g., charging), while also (B) irradiating over the smallest possible cumulative fluence $(e^{-}/Å^{2})$ or shortest time to minimize the magnitude of direct irradiation damage to the polymers. We must be strategic how and when we apply these limited numbers of electrons to our LPTEM sample, where direct structural damage to organics generally is on the order of ca. $10-20~e^-/\text{Å}^2$ fluence total. This is not too restrictive for static LPTEM, comparable to cryo-TEM of polymers, and single-exposure LPTEM imaging of static structures can be done using traditional low-dose imaging methods developed for cryo-TEM, where the structures of interest are only exposed to the beam once, when acquiring the single image, and focusing is done at minimal flux on structures in adjacent regions of liquid cell. 149,232 In static LPTEM, the objective is to acquire a single image of the structure of interest below the direct damage threshold by either using an imageexposure time that is short enough such that indirect chemical damage does not have sufficient time to significantly manifest in the sample or at a flux that is low enough where chemical damage is insignificant during the image acquisition time, providing a true representation of structure's morphology without beam artefacts. That is, we can either use very short exposure time at high flux to try to "beat" the chemical damage that will necessarily occur or use a long exposure time and very low fluence to try to suppress and eliminate chemical damage all together with the help of additives. The optimal static imaging conditions are thus sample dependent. The rate of radiolysis product generation (Figure 6) and the rate at which radiolysis products react with polymers to cause structural damage (Figure 7) will change for different sample concentrations, polymers, solvents, and additives, giving all samples some degree of time and flux dependence. Different TEM cameras are also optimized for imaging at different fluxes per frame, where direct electron counting TEM cameras perform best at low flux (ca. $1-10 \text{ e}^-/\text{pixel s}$ or below)²³³ due to their ability to use rapid frame rates on the order of

hundreds of frames per second and multiframe summing in the acquisition of single images, while traditional charge-coupled device (CCD) cameras perform best at higher flux due to their inherently slow readout speed and comparatively high system noise. $^{234-236}$

In addition to conventional TEM mode, the annular darkfield scanning TEM (STEM) mode can be effective for resolving soft matter structures containing high Z-species, such as Ferritin particles, and will generally achieve better resolution than TEM through thick liquids. 52,237 However, it is important to note that the irradiation conditions and resulting solution radiolysis in STEM mode will be very different than in spreadbeam TEM mode at similar beam current, due to the very high local flux (>10 pA condensed to sub-nm diameter) of the scanning STEM probe and the temporal fluctuation in the application of the local flux in STEM. 41,181,238 Applying the existing LCTEM radiolysis model to STEM irradiation is problematic; the true flux cannot be computed in STEM, as is routine in TEM mode. The acquisition of single STEM images (max ca. 10 fps) is also generally slower than in TEM mode using a CMOS camera (over 1000 fps), and each location within a STEM frame contains signals acquired at slightly different time points, making dynamics difficult to analyze in STEM video data. New subsampling STEM techniques have shown promise for controlling STEM irradiation conditions, ²³⁹ which should allow STEM mode to be more readily applied to beam-sensitive samples of all kinds, including polymers. For most low-density polymer samples in LPTEM, the conventional TEM mode remains the best option for both minimizing beam damage and maximizing contrast or frame rate of polymer nanostructures.

For dynamic LPTEM videography experiments, avoiding or preventing artefactual damage is a far greater challenge.² LPTEM videography requires that the entire series of continuous video frames be recorded below the direct damage fluence threshold, while also requiring operation at an incident flux where chemical damage is mitigated during the entirety of observation. Beating out damage is not viable for videography of any observation period that is several seconds or longer. For videography, preventing chemical damage is paramount, achieved through the use of lower flux and the assistance of radiolysis scavengers. However, each video frame requires a non-zero electron flux to strike the camera, and frames at very low flux per frame on-camera become increasing noisy; even with the best cameras, there is flux per frame minimum below which no meaningful information is contained. Without changing the incident flux per second, the flux per frame oncamera can be increased by increasing the exposure time per frame, thus lowering frame rate. This trade-off between frame signal-to-noise and frame rate leads to either very low contrast structures being unobservable when using fast frame rates or very fast dynamics being unobservable when using slow frame rates. We must optimize our acquisition parameters for the dynamic process of interest, without exceeding the total direct damage fluence threshold or the chemical damage flux rate threshold of the sample.

The TEM camera is thus the most important component of the microscope system in LPTEM; a *better* camera, one with a higher pixel density and that is more sensitive in detecting electron strikes with less noise, allows us to extract the maximum possible information from the necessarily low signal and contrast over background in our LPTEM video frames and images. Indeed, complementary metal-oxide-semiconductor

(CMOS) based direct electron counting cameras provide far superior imaging performance over traditional CCDs, even in the basic static imaging modes, and have unparallel read-out speed for capturing rapid dynamics that demand high frame rate.^{234–236} However, in polymer chemistry and materials synthesis, generally, processes of interest can occur over the minutes to hours time scale, durations far too long to video continuously below the fluence damage threshold. For such long-duration dynamics and processes, LPTEM microscopists have utilized stroboscopic videography methods, where the beam is off, or blanked, between single-image frames spaced over time, and the images are stacked into a video after acquisition. 21 The stroboscopic method allows microscopists to take a time lapse of a discrete process below the fluence damage threshold but produces an observation that is interrupted by gaps of time with no information. This approach has the potential to miss steps within the overall dynamic process.

Post-acquisition image and video processing has become an essential component for analyzing LPTEM data. To mitigate experimental artefacts and sample damage, the best LPTEM data will necessarily contain very low signal with high noise levels and with structures that have very low contrast over background. Such data might be uninterpretable to the naked eye, approaching pure white noise, but can be effectively processed and quantified using modern image processing methods that include dynamic background subtraction, deblurring filters, structure or object thresholding, size-shape quantification, and motion tracking and modeling. 27,46,55,57,59,62,240 Without additional processing, reliable LPTEM data of polymer samples might not be as visually pronounced as one might desire, particularly in comparison to high-resolution TEM images of inorganic structures; however, the true impact lays in insights that can be extracted through careful experimental practice and data analysis of a sample in its solvated state.

SUMMARY OF POTENTIAL LPTEM ARTEFACTS FOR POLYMER SAMPLES AND THE LPTEM EXPERIMENT WORKFLOW

In any LPTEM vessel, window-surface interactions with the solvent and solvated polymers play a much more significant role than they do in normal bulk conditions. These effects can be tuned to some degree by the choice of the window material, plasma treatment, and the addition of coatings or chemical modifications to the surface. As discussed above, when under direct observation via irradiation with the e-beam, the windows of the LPTEM vessel will emit ESEs into solution while becoming deprotonated, effects that generate window charging and electric fields for low conductivity windows, while also progressively altering the window surface composition and its interactions with the polymer sample. Irradiation of the solution causes radiolysis, generating a steady-state concentration of reactive radical and ion species in the vessel that depends on the irradiation flux, energy of incident electrons, and the initial solution chemistry. In an aqueous solution, hydroxyl radicals formed from water radiolysis are known to be highly damaging to solvated polymer molecules. This effect must be mitigated to acquire LPTEM images of polymers that are not plagued by chemical damage and sample degradation. Chemical additives can be used to either scavenge these damaging radiolysis products or to heal damaged polymers,

while control over irradiation flux and fluence can be used to limit the rate and amount of hydroxyl radical production.

Direct irradiation to the polymer molecules themselves is also potentially damaging or artefactual. The extent and form(s) of direct damage can be measured for a polymer sample using pre-LPTEM EELS analysis. For many polymers, damage from hydroxyl radical attack and from direct irradiation can be very similar, resulting in a radical polymer cation that is prone to cross-linking. As a general rule, all polymers are susceptible to cross-linking or gelling during LPTEM; chain scission can be significantly mitigated by deaerating polymer solutions, and only certain polymers suffer scission in the absence of O₂. Continuous carbon backbones are also far more stable against scission than those interrupted with S, N, and O atoms. All else being equal, using a more densely aromatic polymer molecule will increase the polymer's resistance to both direct beam damage and indirect chemical damage. The incorporation of aromatic groups is ideal in the polymers themselves, the solvent, or the additives to reduce all forms of damage during LPTEM.

Finally, with the current instrumentation, we cannot chemically detect beam damage artefacts to our polymer system during any in situ LPTEM imaging or videography experiment. Post mortem methods are critical to understand and quantify the magnitudes and types of damage or to determine LPTEM conditions where such artefacts are reduced or eliminated. However, the videographic LPTEM data itself can also be used as evidence of physical artefacts in the LPTEM system. For example, charging and electric-field artefacts can manifest in the anomalous surface-motion behavior of objects in LPTEM, and this motion can be deconvoluted and quantified semi-empirically though careful analysis of the videographic data.^{241¹} Though the LPTEM workflow that we have described in the sections above, involving rigorous pre and post mortem analysis in addition to the in situ LPTEM experiment itself, requires more steps than conventional cryo-TEM or bulk scattering experiments, LPTEM can be effectively applied to study polymer systems in situ and, if done carefully, can provide unprecedented insight into discrete polymer nanostructures or nanoscale chemical and materials processes in solution.

■ CONCLUSION AND PERSPECTIVES

As we have developed new synthetic routes to precisely control molecular complexity and nanostructures of assembled polymer materials, polymer science in the 21st century has progressed towards solving complex problems at the nanoscale. The resulting nanoscale structures require new characterization methods complementary to existing bulk characterization techniques. To this end, liquid-phase TEM is a promising technique for directly observing structures and nanoscale dynamics in solvated polymeric materials with high spatial and temporal resolution. However, the observation can, of course, never be taken out of the equation. For LPTEM, beam effects cannot be eliminated, and to interpret data properly, it is critical to develop a full understanding of how the beam interacts with the imaging vessel and the entire solution. A better understanding of which specific additives can mitigate sample damage and which techniques can be employed for a post mortem analysis must continue to be developed. Understanding these crucial components of LPTEM will allow this technique to develop into a robust and routine method for analysis of polymers and soft matter assemblies.

Critically, the solution-phase videography enabled by LPTEM provides a direct route to characterizing solvated polymeric materials in a dynamic manner. This has allowed transformations to be examined, including chemical reactions that lead to polymer formation and assembly. In its most basic setting, imaging complex morphologies in the solvated state will be valuable, especially in cases where those morphologies are temperature dependent or where they are in nonaqueous solvent; both conditions are not readily studied by cryo-TEM. Finally, we anticipate the real advances and impact on polymer science will come when scattering methods are employed in tandem with real space solution-phase TEM imaging. This will allow correlative analysis of bulk solution-phase properties and microscopy of individual particles and polymers. Together with advanced machine learning image analysis methods for extracting information from low contrast micrographs, the promise of LPTEM for polymer science becomes limitless. With this array of tools in hand, one imagines unprecedented insight into currently elusive soft matter processes, including the routine imaging of fully solvated hydrogel formation and dynamics or biological disease-associated proteinaceous fiber formation and microtubule seed and growth.

AUTHOR INFORMATION

Corresponding Author

Nathan C. Gianneschi — Department of Chemistry,
International Institute for Nanotechnology, Chemistry of Life
Processes Institute, Simpson Querrey Institute, and
Department of Materials Science & Engineering and
Department of Biomedical Engineering, Northwestern
University, Evanston, Illinois 60208, United States;
orcid.org/0000-0001-9945-5475;

Email: nathan.gianneschi@northwestern.edu

Authors

Lucas R. Parent — Innovation Partnership Building, The University of Connecticut, Storrs, Connecticut 06269, United States

Karthikeyan Gnanasekaran — Department of Chemistry, International Institute for Nanotechnology, Chemistry of Life Processes Institute, Simpson Querrey Institute, and Department of Materials Science & Engineering and Department of Biomedical Engineering, Northwestern University, Evanston, Illinois 60208, United States; orcid.org/0000-0001-6635-0888

Joanna Korpanty — Department of Chemistry, International Institute for Nanotechnology, Chemistry of Life Processes Institute, Simpson Querrey Institute, and Department of Materials Science & Engineering and Department of Biomedical Engineering, Northwestern University, Evanston, Illinois 60208, United States

Complete contact information is available at: https://pubs.acs.org/10.1021/acsmacrolett.0c00595

Author Contributions

The manuscript was written through contributions of all authors.

Notes

The authors declare no competing financial interest.

ACKNOWLEDGMENTS

The authors thank the NSF for support of both the Parent and Gianneschi groups through a joint research grant (CHE-1905270). Furthermore, research in the Gianneschi group was conducted with support under and awarded by DoD through the ARO (W911NF-17-1-0326). K.G. thanks the Human Frontier Science Program for a postdoctoral fellowship (LT000869/2018-C).

REFERENCES

- (1) Patterson, J. P.; Robin, M. P.; Chassenieux, C.; Colombani, O.; O'Reilly, R. K. The Analysis of Solution Self-Assembled Polymeric Nanomaterials. *Chem. Soc. Rev.* **2014**, *43*, 2412–2425.
- (2) Jacques, D. A.; Trewhella, J. Small-Angle Scattering for Structural Biology Expanding the Frontier While Avoiding the Pitfalls. *Protein Sci.* **2010**, *19*, 642–657.
- (3) Li, J.; Jiao, A.; Chen, S.; Wu, Z.; Xu, E.; Jin, Z. Application of the Small-Angle X-Ray Scattering Technique for Structural Analysis Studies: A Review. *J. Mol. Struct.* **2018**, *1165*, 391–400.
- (4) Carvalho, P. M.; Felicio, M. R.; Santos, N. C.; Goncalves, S.; Domingues, M. M. Application of Light Scattering Techniques to Nanoparticle Characterization and Development. *Front. Chem.* **2018**, *6*, 237.
- (5) Franken, L. E.; Boekema, E. J.; Stuart, M. C. A. Transmission Electron Microscopy as a Tool for the Characterization of Soft Materials: Application and Interpretation. *Adv. Sci.* **2017**, *4* (5), 1–9.
- (6) Burrows, N. D.; Penn, R. L. Cryogenic Transmission Electron Microscopy: Aqueous Suspensions of Nanoscale Objects. *Microsc. Microanal.* **2013**, *19* (19), 1542–1553.
- (7) Cheng, Y. Single-Particle Cryo-EM-How Did It Get Here and Where Will It Go. *Science (Washington, DC, U. S.)* **2018**, *361*, 876–880.
- (8) Cui, H.; Hodgdon, T. K.; Kaler, E. W.; Abezgauz, L.; Danino, D.; Lubovsky, M.; Talmon, Y.; Pochan, D. J. Elucidating the Assembled Structure of Amphiphiles in Solution via Cryogenic Transmission Electron Microscopy. *Soft Matter* **2007**, *3*, 945.
- (9) Renaud, J. P.; Chari, A.; Ciferri, C.; Liu, W. T.; Rémigy, H. W.; Stark, H.; Wiesmann, C. Cryo-EM in Drug Discovery: Achievements, Limitations and Prospects. *Nat. Rev. Drug Discovery* **2018**, *17*, 471–492.
- (10) Williams, D. B.; Carter, C. B. Transmission Electron Microscopy: A Textbook for Materials Science; Springer, 2009; Vols. 1–4. DOI: 10.1007/978-0-387-76501-3.
- (11) Liu, Y.; Vancso, G. J. Polymer Single Chain Imaging, Molecular Forces, and Nanoscale Processes by Atomic Force Microscopy: The Ultimate Proof of the Macromolecular Hypothesis. *Prog. Polym. Sci.* **2020**, *104*, 101232.
- (12) Ono, Y.; Kumaki, J. In Situ Real-Time Observation of Polymer Folded-Chain Crystallization by Atomic Force Microscopy at the Molecular Level. *Macromolecules* **2018**, *51* (19), 7629–7636.
- (13) Fukui, T.; Uchihashi, T.; Sasaki, N.; Watanabe, H.; Takeuchi, M.; Sugiyasu, K. Direct Observation and Manipulation of Supramolecular Polymerization by High-Speed Atomic Force Microscopy. *Angew. Chem.* **2018**, *130*, 15691–15696.
- (14) Joens, M. S.; Huynh, C.; Kasuboski, J. M.; Ferranti, D.; Sigal, Y. J.; Zeitvogel, F.; Obst, M.; Burkhardt, C. J.; Curran, K. P.; Chalasani, S. H.; Stern, L. A.; Goetze, B.; Fitzpatrick, J. A. J. Helium Ion Microscopy (HIM) for the Imaging of Biological Samples at Sub-Nanometer Resolution. *Sci. Rep.* **2013**, *3*, 3514.
- (15) Wu, J.; Zhu, X.; West, M. M.; Tyliszczak, T.; Shiu, H. W.; Shapiro, D.; Berejnov, V.; Susac, D.; Stumper, J.; Hitchcock, A. P. High-Resolution Imaging of Polymer Electrolyte Membrane Fuel Cell Cathode Layers by Soft X-Ray Spectro-Ptychography. *J. Phys. Chem. C* 2018, 122, 11709–11719.
- (16) Witte, K.; Späth, A.; Finizio, S.; Donnelly, C.; Watts, B.; Sarafimov, B.; Odstrcil, M.; Guizar-Sicairos, M.; Holler, M.; Fink, R. H.; Raabe, J. From 2D STXM to 3D Imaging: Soft X-Ray Laminography of Thin Specimens. *Nano Lett.* **2020**, *20*, 1305–1314.

- (17) Shapiro, D. A.; Yu, Y. S.; Tyliszczak, T.; Cabana, J.; Celestre, R.; Chao, W.; Kaznatcheev, K.; Kilcoyne, A. L. D.; Maia, F.; Marchesini, S.; Meng, Y. S.; Warwick, T.; Yang, L. L.; Padmore, H. A. Chemical Composition Mapping with Nanometre Resolution by Soft X-Ray Microscopy. *Nat. Photonics* **2014**, *8*, 765–769.
- (18) Wirix, M. J. M.; Bomans, P. H. H.; Friedrich, H.; Sommerdijk, N. A. J. M.; De With, G. Three-Dimensional Structure of P3HT Assemblies in Organic Solvents Revealed by Cryo-TEM. *Nano Lett.* **2014**, *14* (4), 2033–2038.
- (19) Friedrich, H.; Frederik, P. M.; De With, G.; Sommerdijk, N. a J. M. Imaging of Self-Assembled Structures: Interpretation of TEM and Cryo-TEM Images. *Angew. Chem., Int. Ed.* **2010**, 49 (43), 7850–7858. (20) Ross, F. M. *Liquid Cell Electron Microscopy*, 1st ed.; Cambridge University Press: New York, 2016.
- (21) Smith, B. J.; Parent, L. R.; Overholts, A. C.; Beaucage, P. A.; Bisbey, R. P.; Chavez, A. D.; Hwang, N.; Park, C.; Evans, A. M.; Gianneschi, N. C.; Dichtel, W. R. Colloidal Covalent Organic Frameworks. *ACS Cent. Sci.* **2017**, *3*, 58–65.
- (22) Vailonis, K. M.; Gnanasekaran, K.; Powers, X. B.; Gianneschi, N. C.; Jenkins, D. M. Elucidating the Growth of Metal-Organic Nanotubes Combining Isoreticular Synthesis with Liquid-Cell Transmisson Electron Microscopy. *J. Am. Chem. Soc.* **2019**, *141*, 10177–10182.
- (23) Kelley, E. G.; Murphy, R. P.; Seppala, J. E.; Smart, T. P.; Hann, S. D.; Sullivan, M. O.; Epps, T. H. Size Evolution of Highly Amphiphilic Macromolecular Solution Assemblies via a Distinct Bimodal Pathway. *Nat. Commun.* **2014**, *5*, 3599.
- (24) Patterson, J. P.; Kelley, E. G.; Murphy, R. P.; Moughton, A. O.; Robin, M. P.; Lu, A.; Colombani, O.; Chassenieux, C.; Cheung, D.; Sullivan, M. O.; Epps, T. H.; O'Reilly, R. K. Structural Characterization of Amphiphilic Homopolymer Micelles Using Light Scattering, SANS, and Cryo-TEM. *Macromolecules* 2013, 46, 6319–6325.
- (25) Patterson, J. P.; Xu, Y.; Moradi, M.; Sommerdijk, N. A. J. M.; Friedrich, H. CryoTEM as an Advanced Analytical Tool for Materials Chemists. *Acc. Chem. Res.* **2017**, *50*, 1495–1501.
- (26) Xiao, L.; Schultz, Z. D. Spectroscopic Imaging at the Nanoscale: Technologies and Recent Applications. *Anal. Chem.* **2018**, *90*, 440–458.
- (27) Parent, L. R.; Bakalis, E.; Proetto, M.; Li, Y.; Park, C.; Zerbetto, F.; Gianneschi, N. C. Tackling the Challenges of Dynamic Experiments Using Liquid-Cell Transmission Electron Microscopy. *Acc. Chem. Res.* **2018**, *51*, 3–11.
- (28) Wang, M.; Dissanayake, T. U.; Park, C.; Gaskell, K.; Woehl, T. J. Nanoscale Mapping of Nonuniform Heterogeneous Nucleation Kinetics Mediated by Surface Chemistry. *J. Am. Chem. Soc.* **2019**, *141*, 13516–13524.
- (29) Kim, B. H.; Yang, J.; Lee, D.; Choi, B. K.; Hyeon, T.; Park, J. Liquid-Phase Transmission Electron Microscopy for Studying Colloidal Inorganic Nanoparticles. *Adv. Mater.* **2018**, *30*, 1703316.
- (30) Hauwiller, M. R.; Frechette, L. B.; Jones, M. R.; Ondry, J. C.; Rotskoff, G. M.; Geissler, P.; Alivisatos, A. P. Unraveling Kinetically-Driven Mechanisms of Gold Nanocrystal Shape Transformations Using Graphene Liquid Cell Electron Microscopy. *Nano Lett.* **2018**, 18, 5731–5737.
- (31) Wang, M.; Park, C.; Woehl, T. J. Quantifying the Nucleation and Growth Kinetics of Electron Beam Nanochemistry with Liquid Cell Scanning Transmission Electron Microscopy. *Chem. Mater.* **2018**, 30, 7727–7736.
- (32) Luo, B.; Smith, J. W.; Ou, Z.; Chen, Q. Quantifying the Self-Assembly Behavior of Anisotropic Nanoparticles Using Liquid-Phase Transmission Electron Microscopy. *Acc. Chem. Res.* **2017**, *50*, 1125–1133.
- (33) Williamson, M. J.; Tromp, R. M.; Vereecken, P. M.; Hull, R.; Ross, F. M. Dynamic Microscopy of Nanoscale Cluster Growth at the Solid Liquid Interface. *Nat. Mater.* **2003**, *2*, 532–536.
- (34) Kosari, A.; Zandbergen, H.; Tichelaar, F.; Visser, P.; Terryn, H.; Mol, A. Application of in Situ Liquid Cell Transmission Electron Microscopy in Corrosion Studies: A Critical Review of Challenges and Achievements. *Corrosion* **2020**, *76*, 4–17.

- (35) Zhu, G.; Reiner, H.; Cölfen, H.; De Yoreo, J. J. Addressing Some of the Technical Challenges Associated with Liquid Phase S/TEM Studies of Particle Nucleation, Growth and Assembly. *Micron* **2019**, *118*, 35–42.
- (36) Rehn, S. M.; Jones, M. R. New Strategies for Probing Energy Systems with in Situ Liquid-Phase Transmission Electron Microscopy. *ACS Energy Lett.* **2018**, *3*, 1269–1278.
- (37) Chen, Q.; Yuk, J. M.; Hauwiller, M. R.; Park, J.; Dae, K. S.; Kim, J. S.; Alivisatos, A. P. Nucleation, Growth, and Superlattice Formation of Nanocrystals Observed in Liquid Cell Transmission Electron Microscopy. *MRS Bull.* **2020**, *45*, 713–726.
- (38) Unocic, R. R.; Jungjohann, K. L.; Mehdi, B. L.; Browning, N. D.; Wang, C. In Situ Electrochemical Scanning/Transmission Electron Microscopy of Electrode-Electrolyte Interfaces. *MRS Bull.* **2020**, *45*, 738–745.
- (39) Woehl, T. J.; Moser, T.; Evans, J. E.; Ross, F. M. Electron-Beam-Driven Chemical Processes during Liquid Phase Transmission Electron Microscopy. *MRS Bull.* **2020**, *45* (9), 746–753.
- (40) Parent, L. R.; Vratsanos, M.; Jin, B.; De Yoreo, J. J.; Gianneschi, N. C. Chemical and Physical Transformations of Carbon-Based Nanomaterials Observed by Liquid Phase Transmission Electron Microscopy. MRS Bull. 2020, 45, 727–737.
- (41) Wu, H.; Friedrich, H.; Patterson, J. P.; Sommerdijk, N. A. J. M.; Jonge, N. De. Liquid-Phase Electron Microscopy for Soft Matter Science and Biology. *Adv. Mater.* **2020**, *32*, 2001582.
- (42) Mirsaidov, U. M.; Zheng, H.; Casana, Y.; Matsudaira, P. Imaging Protein Structure in Water at 2.7 Nm Resolution by Transmission Electron Microscopy. *Biophys. J.* **2012**, *102*, L15–L17.
- (43) Keskin, S.; De Jonge, N. Reduced Radiation Damage in Transmission Electron Microscopy of Proteins in Graphene Liquid Cells. *Nano Lett.* **2018**, *18*, 7435–7440.
- (44) De Yoreo, J. J.; Sommerdijk, N. A. J. M. Investigating Materials Formation with Liquid-Phase and Cryogenic TEM. *Nat. Rev. Mater.* **2016**, *1*, 1–18.
- (45) Ianiro, A.; Wu, H.; van Rijt, M. M. J.; Vena, M. P.; Keizer, A. D. A.; Esteves, A. C. C.; Tuinier, R.; Friedrich, H.; Sommerdijk, N. A. J. M.; Patterson, J. P. Liquid-Liquid Phase Separation during Amphiphilic Self-Assembly. *Nat. Chem.* **2019**, *11*, 320–328.
- (46) Parent, L. R.; Bakalis, E.; Ramirez-Hernandez, A.; Kammeyer, J. K.; Park, C.; de Pablo, J.; Zerbetto, F.; Patterson, J. P.; Gianneschi, N. C. Directly Observing Micelle Fusion and Growth in Solution by Liquid Cell Transmission Electron Microscopy. *J. Am. Chem. Soc.* **2017**, *139*, 17140–17151.
- (47) Patterson, J. P.; Abellan, P.; Denny, M. S.; Park, C.; Browning, N. D.; Cohen, S. M.; Evans, J. E.; Gianneschi, N. C. Observing the Growth of Metal-Organic Frameworks by in Situ Liquid Cell Transmission Electron Microscopy. *J. Am. Chem. Soc.* **2015**, *137*, 7322–7328.
- (48) Park, J.; Park, H.; Ercius, P.; Pegoraro, A. F.; Xu, C.; Kim, J. W.; Han, S. H.; Weitz, D. A. Direct Observation of Wet Biological Samples by Graphene Liquid Cell Transmission Electron Microscopy. *Nano Lett.* **2015**, *15*, 4737–4744.
- (49) Touve, M. A.; Carlini, A. S.; Gianneschi, N. C. Self-Assembling Peptides Imaged by Correlated Liquid Cell Transmission Electron Microscopy and MALDI-Imaging Mass Spectrometry. *Nat. Commun.* **2019**, *10* (1), 1–12.
- (50) Yamazaki, T.; Kimura, Y.; Vekilov, P. G.; Furukawa, E.; Shirai, M.; Matsumoto, H.; Van Driessche, A. E. S.; Tsukamoto, K. Two Types of Amorphous Protein Particles Facilitate Crystal Nucleation. *Proc. Natl. Acad. Sci. U. S. A.* **2017**, *114* (9), 2154–2159.
- (51) Proetto, M. T.; Rush, A. M.; Chien, M. P.; Abellan Baeza, P.; Patterson, J. P.; Thompson, M. P.; Olson, N. H.; Moore, C. E.; Rheingold, A. L.; Andolina, C.; Millstone, J.; Howell, S. B.; Browning, N. D.; Evans, J. E.; Gianneschi, N. C. Dynamics of Soft Nanomaterials Captured by Transmission Electron Microscopy in Liquid Water. *J. Am. Chem. Soc.* **2014**, *136*, 1162–1165.
- (52) Evans, J. E.; Jungjohann, K. L.; Wong, P. C. K.; Chiu, P. L.; Dutrow, G. H.; Arslan, I.; Browning, N. D. Visualizing Macro-

- molecular Complexes with in Situ Liquid Scanning Transmission Electron Microscopy. *Micron* **2012**, *43*, 1085–1090.
- (53) Peckys, D. B.; Macías-Sánchez, E.; de Jonge, N. Liquid Phase Electron Microscopy of Biological Specimens. *MRS Bull.* **2020**, *45* (9), 754–760.
- (54) Smith, J. W.; Chen, Q. Liquid-Phase Electron Microscopy Imaging of Cellular and Biomolecular Systems. *J. Mater. Chem. B* **2020**, 8 (2018), 8490–8506.
- (55) Nagamanasa, K. H.; Wang, H.; Granick, S. Liquid-Cell Electron Microscopy of Adsorbed Polymers. *Adv. Mater.* **2017**, *29*, 1703555.
- (56) Liu, J.; Wei, B.; Sloppy, J. D.; Ouyang, L.; Ni, C.; Martin, D. C. Direct Imaging of the Electrochemical Deposition of Poly(3,4-Ethylenedioxythiophene) by Transmission Electron Microscopy. *ACS Macro Lett.* **2015**, *4*, 897–900.
- (57) Touve, M. A.; Figg, C. A.; Wright, D. B.; Chiwoo, P.; Cantlon, J.; Sumerlin, B. S.; Gianneschi, N. C. Polymerization-Induced Self-Assembly of Micelles Observed by Liquid Cell Transmission Electron Microscopy. ACS Cent. Sci. 2018, 4, 543–547.
- (58) Cookman, J.; Hamilton, V.; Price, L. S.; Hall, S. R.; Bangert, U. Visualising Early-Stage Liquid Phase Organic Crystal Growth via Liquid Cell Electron Microscopy. *Nanoscale* **2020**, *12*, 4636–4644.
- (59) Li, C.; Tho, C. C.; Galaktionova, D.; Chen, X.; Král, P.; Mirsaidov, U. M. Dynamics of Amphiphilic Block Copolymers in an Aqueous Solution: Direct Imaging of Micelle Formation and Nanoparticle Encapsulation. *Nanoscale* **2019**, *11*, 2299–2305.
- (60) Early, J. T.; Yager, K. G.; Lodge, T. P. Direct Observation of Micelle Fragmentation via in Situ Liquid-Phase Transmission Electron Microscopy. *ACS Macro Lett.* **2020**, *9*, 756–761.
- (61) Piffoux, M.; Ahmad, N.; Nelayah, J.; Wilhelm, C.; Silva, A.; Gazeau, F.; Alloyeau, D. Monitoring the Dynamics of Cell-Derived Extracellular Vesicles at the Nanoscale by Liquid-Cell Transmission Electron Microscopy. *Nanoscale* **2018**, *10*, 1234–1244.
- (62) Gnanasekaran, K.; Chang, H.; Smeets, P. J. M.; Korpanty, J.; Geiger, F. M.; Gianneschi, N. C. In Situ Ni2+ Stain for Liposome Imaging by Liquid-Cell Transmission Electron Microscopy. *Nano Lett.* **2020**, 20, 4292–4297.
- (63) de Jonge, N.; Ross, F. M. Electron Microscopy of Specimens in Liquid. *Nat. Nanotechnol.* **2011**, *6*, 695–704.
- (64) Tsuda, T.; Seino, S.; Kuwabata, S. Gold Nanoparticles Prepared with a Room-Temperature Ionic Liquid-Radiation Irradiation Method. *Chem. Commun.* **2009**, *44*, 6792–6794.
- (65) Huang, J. Y.; Zhong, L.; Wang, C. M.; Sullivan, J. P.; Xu, W.; Zhang, L. Q.; Mao, S. X.; Hudak, N. S.; Liu, X. H.; Subramanian, A.; Fan, H.; Qi, L.; Kushima, A.; Li, J. In Situ Observation of the Electrochemical Lithiation of a Single SnO2 Nanowire Electrode. *Science* 2010, 330, 1515–1520.
- (66) Fan, Z.; Zhang, L.; Baumann, D.; Mei, L.; Yao, Y.; Duan, X.; Shi, Y.; Huang, J.; Huang, Y.; Duan, X. In Situ Transmission Electron Microscopy for Energy Materials and Devices. *Adv. Mater.* **2019**, *31*, 1–22.
- (67) Keller, D.; Henninen, T. R.; Erni, R. Formation of Gold Nanoparticles in a Free-Standing Ionic Liquid Triggered by Heat and Electron Irradiation. *Micron* **2019**, *117*, 16–21.
- (68) Tsuda, T.; Sakamoto, T.; Nishimura, Y.; Seino, S.; Imanishi, A.; Kuwabata, S. Various Metal Nanoparticles Produced by Accelerated Electron Beam Irradiation of Room-Temperature Ionic Liquid. *Chem. Commun.* **2012**, *48*, 1925–1927.
- (69) Kimura, Y.; Niinomi, H.; Tsukamoto, K.; García-Ruiz, J. M. In Situ Live Observation of Nucleation and Dissolution of Sodium Chlorate Nanoparticles by Transmission Electron Microscopy. *J. Am. Chem. Soc.* **2014**, *136*, 1762–1765.
- (70) de Jonge, N.; Houben, L.; Dunin-Borkowski, R. E.; Ross, F. M. Resolution and Aberration Correction in Liquid Cell Transmission Electron Microscopy. *Nat. Rev. Mater.* **2019**, *4*, 61–78.
- (71) Li, M.; Knibbe, R. A Study of Membrane Impact on Spatial Resolution of Liquid in Situ Transmission Electron Microscope. *Microsc. Microanal.* **2020**, *26*, 126–133.
- (72) Minamimoto, H.; Irie, H.; Uematsu, T.; Tsuda, T.; Imanishi, A.; Seki, S.; Kuwabata, S. Polymerization of Room-Temperature Ionic

- Liquid Monomers by Electron Beam Irradiation with the Aim of Fabricating Three-Dimensional Micropolymer/Nanopolymer Structures. *Langmuir* **2015**, *31*, 4281–4289.
- (73) Levin, B. D. A.; Haiber, D.; Liu, Q.; Crozier, P. A. An Open-Cell Environmental Transmission Electron Microscopy Technique for in Situ Characterization of Samples in Aqueous Liquid Solutions. *Microsc. Microanal.* **2020**, *26*, 134–138.
- (74) Textor, M.; de Jonge, N. Strategies for Preparing Graphene Liquid Cells for Transmission Electron Microscopy. *Nano Lett.* **2018**, 18, 3313–3321.
- (75) Yuk, J. M.; Park, J.; Ercius, P.; Kim, K.; Hellebusch, D. J.; Crommie, M. F.; Lee, J. Y.; Zettl, A.; Alivisatos, a. P. High-Resolution EM of Colloidal Nanocrystal Growth Using Graphene Liquid Cells. *Science* **2012**, *336*, 61–64.
- (76) Cho, H.; Jones, M. R.; Nguyen, S. C.; Hauwiller, M. R.; Zettl, A.; Alivisatos, A. P. The Use of Graphene and Its Derivatives for Liquid-Phase Transmission Electron Microscopy of Radiation-Sensitive Specimens. *Nano Lett.* **2017**, *17*, 414–420.
- (77) Zhang, J.; Lin, L.; Sun, L.; Huang, Y.; Koh, A. L.; Dang, W.; Yin, J.; Wang, M.; Tan, C.; Li, T.; Tan, Z.; Liu, Z.; Peng, H. Clean Transfer of Large Graphene Single Crystals for High-Intactness Suspended Membranes and Liquid Cells. *Adv. Mater.* **2017**, 29, 1700639.
- (78) Deursen, P. M. G.; Koning, R. I.; Tudor, V.; Moradi, M.-A.; Patterson, J. P.; Kros, A.; Sommerdijk, N. A. J. M.; Koster, A. J.; Schneider, G. F. Graphene Liquid Cells Assembled through Loop-Assisted Transfer Method and Located with Correlated Light-Electron Microscopy. *Adv. Funct. Mater.* **2020**, *30*, 1904468.
- (79) Rasool, H.; Dunn, G.; Fathalizadeh, A.; Zettl, A. Graphene-Sealed Si/SiN Cavities for High-Resolution in Situ Electron Microscopy of Nano-Confined Solutions. *Phys. Status Solidi B* **2016**, 253, 2351–2354.
- (80) Hauwiller, M. R.; Ondry, J. C.; Alivisatos, A. P. Using Graphene Liquid Cell Transmission Electron Microscopy to Study in Situ Nanocrystal Etching. *J. Visualized Exp.* **2018**, *135*, No. e57665.
- (81) Sasaki, Y.; Kitaura, R.; Yuk, J. M.; Zettl, A.; Shinohara, H. Efficient Preparation of Graphene Liquid Cell Utilizing Direct Transfer with Large-Area Well-Stitched Graphene. *Chem. Phys. Lett.* **2016**, *650*, 107–112.
- (82) Hackley, V. A.; Malghan, S. G. The Surface Chemistry of Silicon Nitride Powder in the Presence of Dissolved Ions. *J. Mater. Sci.* **1994**, 29, 4420–4430.
- (83) Greil, P.; Nitzsche, R.; Friedrich, H.; Hermel, W. Evaluation of Oxygen Content on Silicon Nitride Powder Surface from the Measurement of the Isoelectric Point. *J. Eur. Ceram. Soc.* **1991**, *7*, 353–359.
- (84) Raider, S. I.; Flitsch, R.; Aboaf, J. A.; Pliskin, W. A. Surface Oxidation of Silicon Nitride Films. *J. Electrochem. Soc.* **1976**, 123, 560–565
- (85) Morita, M.; Ohmi, T.; Hasegawa, E.; Kawakami, M.; Ohwada, M. Growth of Native Oxide on a Silicon Surface. *J. Appl. Phys.* **1990**, 68, 1272–1281.
- (86) Stadelmann, H.; Petzow, G.; Greil, P. Effects of Surface Purification on the Properties of Aqueous Silicon Nitride Suspensions. *J. Eur. Ceram. Soc.* **1989**, *5*, 155–163.
- (87) Sonnefeld, J. Determination of Surface Charge Density Parameters of Silicon Nitride. *Colloids Surf.*, A 1996, 108, 27–31.
- (88) Cloarec, J. P.; Chevalier, C.; Genest, J.; Beauvais, J.; Chamas, H.; Chevolot, Y.; Baron, T.; Souifi, A. PH Driven Addressing of Silicon Nanowires onto Si3N4/SiO2Micro-Patterned Surfaces. *Nanotechnology* **2016**, *27*, 295602–295610.
- (89) Stine, R.; Cole, C. L.; Ainslie, K. M.; Mulvaney, S. P.; Whitman, L. J. Formation of Primary Amines on Silicon Nitride Surfaces: A Direct, Plasma-Based Pathway to Functionalization. *Langmuir* **2007**, 23, 4400–4404.
- (90) Mezzasalma, S.; Baldovino, D. Characterization of Silicon Nitride Surface in Water and Acid Environment: A General Approach to the Colloidal Suspensions. *J. Colloid Interface Sci.* **1996**, *180*, 413–420.

- (91) Bland, H. A.; Thomas, E. L. H.; Klemencic, G. M.; Mandal, S.; Morgan, D. J.; Papageorgiou, A.; Jones, T. G.; Williams, O. A. Superconducting Diamond on Silicon Nitride for Device Applications. *Sci. Rep.* **2019**, *9*, 2911–2919.
- (92) Rao, R. R.; Roopa, H. N.; Kannan, T. S. PH Controlled Dispersion and Slip Casting of Si3N4 in Aqueous Media. *Bull. Mater. Sci.* **2001**, *24*, 57–61.
- (93) Stephan, A. C.; Finot, E. L.; Ji, H. F.; Pinnaduwage, L. A.; Thundat, T. Micromechanical Measurement of Active Sites on Silicon Nitride Using Surface Free Energy Variation. *Ultramicroscopy* **2002**, *91*, 1–8.
- (94) Zhuravlev, L. T. The Surface Chemistry of Amorphous Silica. Zhuravlev Model. *Colloids Surf.*, A **2000**, 173, 1–38.
- (95) Robertson, A. W.; Zhu, G.; Mehdi, B. L.; Jacobs, R. M. J.; De Yoreo, J.; Browning, N. D. Nanoparticle Immobilization for Controllable Experiments in Liquid-Cell Transmission Electron Microscopy. ACS Appl. Mater. Interfaces 2018, 10, 22801–22808.
- (96) Kashyap, S.; Woehl, T. J.; Liu, X.; Mallapragada, S. K.; Prozorov, T. Nucleation of Iron Oxide Nanoparticles Mediated by Mms6 Protein in Situ. *ACS Nano* **2014**, *8*, 9097–9106.
- (97) Woehl, T. J.; Kashyap, S.; Firlar, E.; Perez-Gonzalez, T.; Faivre, D.; Trubitsyn, D.; Bazylinski, D. A.; Prozorov, T. Correlative Electron and Fluorescence Microscopy of Magnetotactic Bacteria in Liquid: Toward in Vivo Imaging. *Sci. Rep.* **2015**, *4*, 22–29.
- (98) Kennedy, G. P.; Buiu, O.; Taylor, S. Oxidation of Silicon Nitride Films in an Oxygen Plasma. *J. Appl. Phys.* **1999**, 85, 3319–3326
- (99) Aronsson, B. O.; Lausmaa, J.; Kasemo, B. Glow Discharge Plasma Treatment for Surface Cleaning and Modification of Metallic Biomaterials. *J. Biomed. Mater. Res.* **1997**, *35*, 49–73.
- (100) Belkind, A.; Gershman, S. Plasma Cleaning of Surfaces. *Vaccum Technol. Coat.* **2008**, 1–11.
- (101) Li-Te Yin; Jung-Chuan Chou; Wen-Yaw Chung; Tai-Ping Sun; Shen-Ken Hsiung. Characteristics of Silicon Nitride after O2 Plasma Surface Treatment for PH-ISFET Applications. *IEEE Trans. Biomed. Eng.* **2001**, *48*, 340–344.
- (102) Duval, Y.; Mielczarski, J. A.; Pokrovsky, O. S.; Mielczarski, E.; Ehrhardt, J. J. Evidence of the Existence of Three Types of Species at the Quartz-Aqueous Solution Interface at PH 0-10: XPS Surface Group Quantification and Surface Complexation Modeling. *J. Phys. Chem. B* **2002**, *106*, 2937–2945.
- (103) Arafat, A.; Schroën, K.; De Smet, L. C. P. M.; Sudhölter, E. J. R.; Zuilhof, H. Tailor-Made Functionalization of Silicon Nitride Surfaces. *J. Am. Chem. Soc.* **2004**, *126*, 8600–8601.
- (104) Brunet, M.; Aureau, D.; Chantraine, P.; Guillemot, F.; Etcheberry, A.; Gouget-Laemmel, A. C.; Ozanam, F. Etching and Chemical Control of the Silicon Nitride Surface. *ACS Appl. Mater. Interfaces* **2017**, *9*, 3075–3084.
- (105) Luhmann, N.; Jachimowicz, A.; Schalko, J.; Sadeghi, P.; Sauer, M.; Foelske-Schmitz, A.; Schmid, S. Effect of Oxygen Plasma on Nanomechanical Silicon Nitride Resonators. *Appl. Phys. Lett.* **2017**, *111*, 063103–063106.
- (106) Raiteri, R.; Margesin, B.; Grattarola, M. An Atomic Force Microscope Estimation of the Point of Zero Charge of Silicon Insulators. *Sens. Actuators, B* **1998**, *46*, 126–132.
- (107) Dukes, M. J.; Peckys, D. B.; Jonge, N. De; de Jonge, N. Correlative Fluorescence Microscopy and Scanning Transmission Electron Microscopy of Quantum-Dot-Labeled Proteins in Whole Cells in Liquid. *ACS Nano* **2010**, *4*, 4110–4116.
- (108) Hermannsdörfer, J.; Tinnemann, V.; Peckys, D. B.; de Jonge, N. The Effect of Electron Beam Irradiation in Environmental Scanning Transmission Electron Microscopy of Whole Cells in Liquid. *Microsc. Microanal.* **2016**, 22, 656–665.
- (109) Colic, M.; Franks, G.; Fisher, M.; Lange, F. Chemisorption of Organofunctional Silanes on Silicon Nitride for Improved Aqueous Processing. *J. Am. Ceram. Soc.* **1998**, *81*, 2157–2163.
- (110) Hamlett, C. A. E.; Critchley, K.; Gorzny, M.; Evans, S. D.; Prewett, P. D.; Preece, J. A. Vapour Phase Formation of Amino Functionalised Si3N4 Surfaces. *Surf. Sci.* **2008**, *602*, 2724–2733.

- (111) Egerton, R. F. Electron Energy-Loss Spectroscopy in the Electron Microscope, 2nd ed.; Spinger Science + Business Media, LLC, 1996.
- (112) Angert, I.; Burmester, C.; Dinges, C.; Rose, H.; Schroder, R. R. Elastic and Inelastic Scattering Cross-Sections of Amorphous Layers of Carbon and Vitrified Ice. *Ultramicroscopy* **1996**, *63*, 181–192.
- (113) de Jonge, N. Theory of the Spatial Resolution of (Scanning) Transmission Electron Microscopy in Liquid Water or Ice Layers. *Ultramicroscopy* **2018**, *187*, 113–125.
- (114) Reimer, L.; Ross-Messemer, M. Contrast in the Electron Spectroscopic Imaging Mode of a TEM. I. Influence of Zero-loss Filtering on Scattering Contrast. J. Microsc. 1989, 155, 169–182.
- (115) de Jonge, N. Theory of the Spatial Resolution of (Scanning) Transmission Electron Microscopy in Liquid Water or Ice Layers. *Ultramicroscopy* **2018**, *187*, 113–125.
- (116) Keskin, S.; Kunnas, P.; De Jonge, N. Liquid-Phase Electron Microscopy with Controllable Liquid Thickness. *Nano Lett.* **2019**, *19*, 4608–4613.
- (117) Van Omme, J. T.; Wu, H.; Sun, H.; Beker, A. F.; Lemang, M.; Spruit, R. G.; Maddala, S. P.; Rakowski, A.; Friedrich, H.; Patterson, J. P.; Pérez Garza, H. H. Liquid Phase Transmission Electron Microscopy with Flow and Temperature Control. *J. Mater. Chem. C* **2020**, *8*, 10781–10790.
- (118) Egerton, R. F. Mechanisms of Radiation Damage in Beam-Sensitive Specimens, for TEM Accelerating Voltages between 10 and 300 KV. *Microsc. Res. Tech.* **2012**, *75*, 1550–1556.
- (119) Egerton, R. F.; McLeod, R.; Wang, F.; Malac, M. Basic Questions Related to Electron-Induced Sputtering in the TEM. *Ultramicroscopy* **2010**, *110*, 991–997.
- (120) Meyer, J. C.; Eder, F.; Kurasch, S.; Skakalova, V.; Kotakoski, J.; Park, H. J.; Roth, S.; Chuvilin, A.; Eyhusen, S.; Benner, G.; Krasheninnikov, A. V.; Kaiser, U. Accurate Measurement of Electron Beam Induced Displacement Cross Sections for Single-Layer Graphene. *Phys. Rev. Lett.* **2012**, *108*, 196102–196106.
- (121) Wang, H.; Hima Nagamanasa, K.; Kim, Y. J.; Kwon, O. H.; Granick, S. Longer-Lasting Electron-Based Microscopy of Single Molecules in Aqueous Medium. *ACS Nano* **2018**, *12*, 8572–8578.
- (122) Robertson, A. W.; Warner, J. H. Atomic Resolution Imaging of Graphene by Transmission Electron Microscopy. *Nanoscale* **2013**, *5*, 4079–4093.
- (123) Jiang, N. Damage Mechanisms in Electron Microscopy of Insulating Materials. *J. Phys. D: Appl. Phys.* **2013**, *46*, 305502–305506.
- (124) Russo, C. J.; Henderson, R. Charge Accumulation in Electron Cryomicroscopy. *Ultramicroscopy* **2018**, *187*, 43–49.
- (125) Cazaux, J. Correlations between Ionization Radiation Damage and Charging Effects in Transmission Electron Microscopy. *Ultramicroscopy* **1995**, *60* (3), 411–425.
- (126) Egerton, R. F.; Li, P.; Malac, M. Radiation Damage in the TEM and SEM. *Micron* 2004, 35, 399-409.
- (127) Seiler, H. Secondary Electron Emission in the Scanning Electron Microscope. *J. Appl. Phys.* **1983**, *54*, R1–R18.
- (128) Tolias, P. On Secondary Electron Emission and Its Semi-Empirical Description. *Plasma Phys. Controlled Fusion* **2014**, *56*, 123002–123010.
- (129) Xie, A. G.; Lai, M.; Chen, Y. L.; Xia, Y. Q. Formulae for Secondary Electron Yield from Insulators and Semiconductors. *Nucl. Sci. Tech.* **2017**, 28, 18–23.
- (130) Kanaya, K.; Kawakatsu, H. Secondary Electron Emission Due to Primary and Backscattered Electrons. *J. Phys. D: Appl. Phys.* **1972**, *5*, 1727–1742.
- (131) Joy, D. C. A Model for Calculating Secondary and Backscattered Electron Yields. *J. Microsc.* **1987**, *147*, 51–64.
- (132) Lin, Y.; Joy, D. C. A New Examination of Secondary Electron Yield Data. Surf. Interface Anal. 2005, 37, 895–900.
- (133) Cazaux, J. A Physical Approach to the Radiation Damage Mechanisms Induced by X- Rays in X-Ray Microscopy and Related Techniques. J. Microsc. 1997, 188, 106–124.

- (134) Cazaux, J. Correlations between Ionization Radiation Damage and Charging Effects in Transmission Electron Microscopy. *Ultramicroscopy* **1995**, *60*, 411–425.
- (135) Le Caër, S. Water Radiolysis: Influence of Oxide Surfaces on H2 Production under Ionizing Radiation. *Water* **2011**, *3*, 235–253.
- (136) Chelnokov, E.; Cuba, V.; Simeone, D.; Guigner, J. M.; Schmidhammer, U.; Mostafavi, M.; Le Caër, S. Electron Transfer at Oxide/Water Interfaces Induced by Ionizing Radiation. *J. Phys. Chem.* C 2014, 118, 7865–7873.
- (137) Dimitrijevic, N. M.; Henglein, A.; Meisel, D. Charge Separation across the Silica Nanoparticle/Water Interface. *J. Phys. Chem. B* **1999**, *103*, 7073–7076.
- (138) Ouerdane, H.; Gervais, B.; Zhou, H.; Beuve, M.; Renault, J. P. Radiolysis of Water Confined in Porous Silica: A Simulation Study of the Physicochemical Yields. *J. Phys. Chem. C* **2010**, *114*, 12667–12674.
- (139) Abellan, P.; Woehl, T. J. Liquid Cell Electron Microscopy for the Study of Growth Dynamics of Nanomaterials and Structure of Soft Matter. *In In-situ Characterization Techniques for Nanomaterials* **2018**, 1–31.
- (140) Jiang, N. Note on in Situ (Scanning) Transmission Electron Microscopy Study of Liquid Samples. *Ultramicroscopy* **2017**, 179, 81–
- (141) Jiang, N. Beam Damage by the Induced Electric Field in Transmission Electron Microscopy. *Micron* **2016**, 83, 79–92.
- (142) Milosavljevic, B. H.; Pimblott, S. M.; Meisel, D. Yields and Migration Distances of Reducing Equivalents in the Radiolysis of Silica Nanoparticles. *J. Phys. Chem. B* **2004**, *108*, 6996–7001.
- (143) Brodie-Linder, N.; Le Caër, S.; Alam, M. S.; Renault, J. P.; Alba-Simionesco, C. H2 Formation by Electron Irradiation of SBA-15 Materials and the Effect of CuII Grafting. *Phys. Chem. Chem. Phys.* **2010**, *12*, 14188–14195.
- (144) Brunet, F.; Charpentier, T.; Le Caër, S.; Renault, J. P. Solid-State NMR Characterization of a Controlled-Pore Glass and of the Effects of Electron Irradiation. *Solid State Nucl. Magn. Reson.* **2008**, *33*, 1–11.
- (145) De Penhoat, M. A. H.; Goulet, T.; Frongillo, Y.; Fraser, M. J.; Bernat, P.; Jay-Gerin, J. P. Radiolysis of Liquid Water at Temperatures up to 300 °C: A Monte Carlo Simulation Study. *J. Phys. Chem. A* **2000**, *104*, 11757–11770.
- (146) Bobowski, K. Radiation Chemistry of Liquid Systems. In Applications of Ionizing Radiation in Materials Processing 2017, 81–116.
- (147) Schneider, N. M.; Norton, M. M.; Mendel, B. J.; Grogan, J. M.; Ross, F. M.; Bau, H. H. Electron Water Interactions and Implications for Liquid Cell Electron Microscopy. *J. Phys. Chem. C* **2014**, *118*, 22373–22382.
- (148) WOEHL, T.J.; ABELLAN, P. Defining the Radiation Chemistry during Liquid Cell Electron Microscopy to Enable Visualization of Nanomaterial Growth and Degradation Dynamics. *J. Microsc.* **2017**, *265*, 135–147.
- (149) Moser, T. H.; Mehta, H.; Park, C.; Kelly, R. T.; Shokuhfar, T.; Evans, J. E. The Role of Electron Irradiation History in Liquid Cell Transmission Electron Microscopy. *Sci. Adv.* **2018**, *4*, No. eaaq1202.
- (150) Wang, S. T.; Lin, Y.; Nielsen, M. H.; Song, C. Y.; Thomas, M. R.; Spicer, C. D.; Kröger, R.; Ercius, P.; Aloni, S.; Stevens, M. M. Shape-Controlled Synthesis and: In Situ Characterisation of Anisotropic Au Nanomaterials Using Liquid Cell Transmission Electron Microscopy. *Nanoscale* 2019, 11, 16801–16809.
- (151) Gupta, T.; Schneider, N. M.; Park, J. H.; Steingart, D.; Ross, F. M. Spatially Dependent Dose Rate in Liquid Cell Transmission Electron Microscopy. *Nanoscale* **2018**, *10*, 7702–7710.
- (152) Meesungnoen, J.; Jay-Gerin, J. P.; Filali-Mouhim, A.; Mankhetkorn, S. Low-Energy Electron Penetration Range in Liquid Water. *Radiat. Res.* **2002**, *158*, 657–660.
- (153) Berger, M. J.; Coursey, J. S.; Zucker, M. A.; Change, J. NIST Stopping-Power and Range Tables: Electrons, Protons, Helium Ions. http://www.nist.gov/pml/data/star/index.cfm/ (accessed Jun 27, 2014).

- (154) Ambrožič, B.; Prašnikar, A.; Hodnik, N.; Kostevšek, N.; Likozar, B.; Rožman, K. Ž.; Šturm, S. Controlling the Radical-Induced Redox Chemistry inside a Liquid-Cell TEM. *Chem. Sci.* **2019**, *10*, 8735–8743.
- (155) Baxendale, J. H.; Wardman, P. Radiolysis of Methanol: Product Yields, Rate Constants, and Spectroscopic Parameters of Intermediates; National Bureau of Standards, U.S. Department of Commerce, 1975; Vol. 54. DOI: 10.6028/NBS.NSRDS.54.
- (156) Tolbert, B. M.; Krinks, M. H. Chemical Effects of Ionizing Radiation on Pure Organic Compounds. *Radiat. Res., Suppl.* **1960**, *2*, 710–712.
- (157) Choi, S. U.; Lichtin, N. N. The Radiolysis of Methanol and Methanolic Solutions. III, The Effect of Oxygen on the Radiolysis of Liquid Methanol by 60Co γ -Rays and by B(n, α)Li Recoils. *J. Am. Chem. Soc.* **1964**, *86*, 3948–3953.
- (158) Grollmann, U.; Schnabel, W. On the Kinetics of Polymer Degredation in Solution, 9 Pulse Radiolysis of Poly(Ethylene Oxide). *Makromol. Chem.* **1980**, *181*, 1215–1226.
- (159) Billany, M. R.; Khatib, K.; Gordon, M.; Sugden, J. K. Alcohols and Ethanolamines as Hydroxyl Radical Scavengers. *Int. J. Pharm.* **1996**, *137*, 143–147.
- (160) Wang, H.; Nagamanasa, K. H.; Kim, Y.-J.; Kwon, O.-H.; Granick, S. Longer-Lasting Electron-Based Microscopy of Single Molecules in Aqueous Medium. *ACS Nano* **2018**, *12*, 8572–8578.
- (161) Charlesby, A.; Feydelor, P. J.; Kopp, P. M.; Keene, J. P.; Swallow, A. J. Pulse Radiolysis Studies of Aqueous Polymer-Thiourea Systems. *In Pulse Radiolysis* **1965**, 193–201.
- (162) Armstrong, R. C. Correlation of Results from Pulse Radiolysis and Gamma-Radiation: Repair Processes in a Macromolecule Irradiated in Solution. *Int. J. Radiat. Biol. Relat. Stud. Phys., Chem. Med.* **1969**, *16*, 197–200.
- (163) Grollmann, U.; Schnabel, W. On the Kinetics of Polymer Degradation in Solution, Pulse Radiolysis of Poly(Ethylene Oxide). *Makromol. Chem.* **1980**, *181*, 1215–1226.
- (164) Grollmann, U.; Schnabel, W. Free Radical-Induced Oxidative Degradation of Polyacrylamide in Aqueous Solution. *Polym. Degrad. Stab.* **1982**, *4*, 203–212.
- (165) Bhardwaj, Y. K.; Mohan, H.; Sabharwal, S.; Mukherjee, T. Radiation Effect on Poly (p-Sodium Styrene Sulphonate) of Different Degrees of Polymerization in Aqueous Solution: Pulse Radiolysis and Steady State Study. *Radiat. Phys. Chem.* **2001**, *62*, 229–242.
- (166) Swallow, A. J. Pulse Radiolysis of Monomers and Polymers. Adv. Chem. Ser. 1968, 82, 499-512.
- (167) Dispenza, C.; Alessi, S.; Spadaro, G. Radiation Processing of Polymers in Aqueous Media. In *Applications of ionizing radiation in materials processing*; Instytut Chemii i Techniki Jadrowej, pp 291–326
- (168) Garrison, W. M. Reaction Mechanisms in the Radiolysis of Peptides, Polypeptides, and Proteins. *Chem. Rev.* **1987**, *87*, 381–398.
- (169) Von Sonntag, C. Free-Radical-Induced Chain Scission and Cross-Linking of Polymers in Aqueous Solution An Overview. *Radiat. Phys. Chem.* **2003**, *67*, 353–359.
- (170) Berndt, T.; Böge, O. Gas-Phase Reaction of OH Radicals with Benzene: Products and Mechanism. *Phys. Chem. Chem. Phys.* **2001**, *3*, 4946–4956.
- (171) Klotz, B.; Barnes, I.; Golding, B. T.; Becker, K.-H. Atmospheric Chemistry of Toluene-1, 2-Oxide / 2-Methyloxepin. *Phys. Chem. Chem. Phys.* **2000**, 2, 227–235.
- (172) Kovacevic, G.; Sabljic, A. Mechanisms and Reaction-Path Dynamics of Hydroxyl Radical Reactions with Aromatic Hydrocarbons: The Case of Chlorobenzene. *Chemosphere* **2013**, 92, 851–856.
- (173) Davenas, J.; Stevenson, I.; Celette, N.; Cambon, S.; Gardette, J. L.; Rivaton, A.; Vignoud, L. Stability of Polymers under Ionising Radiation: The Many Faces of Radiation Interactions with Polymers. *Nucl. Instrum. Methods Phys. Res., Sect. B* **2002**, *191*, 653–661.
- (174) Kornacka, E. Radiation-Induced Oxidation of Polymers. *In Applications of Ionizing Radiation in Materials Processing* **2017**, 183–192.

- (175) Chapiro, A. Chemical Modifications in Irradiated Polymers. *Nucl. Instrum. Methods Phys. Res., Sect. B* **1988**, 32, 111–114.
- (176) Ventura, A.; Ngono-Ravache, Y.; Marie, H.; Levavasseur-Marie, D.; Legay, R.; Dauvois, V.; Chenal, T.; Visseaux, M.; Balanzat, E. Hydrogen Emission and Macromolecular Radiation-Induced Defects in Polyethylene Irradiated under an Inert Atmosphere: The Role of Energy Transfers toward Trans-Vinylene Unsaturations. *J. Phys. Chem. B* **2016**, *120*, 10367–10380.
- (177) Sun, Y.; Boggs, S. A.; Ramprasad, R. Monte Carlo Studies of Hot Electron Transport and High Field Degradation. 2014 IEEE Conf. Electr. Insul. Dielectr. Phenomena, CEIDP 2014 2014, 15–18.
- (178) Wang, C.; Duscher, G.; Paddison, S. J. Electron Energy Loss Spectroscopy of Polytetrafluoroethylene: Experiment and First Principles Calculations. *Microscopy* **2014**, *63*, 73–83.
- (179) Varlot, K.; Martin, J. M.; Gonbeau, D.; Quet, C. Chemical Bonding Analysis of Electron-Sensitive Polymers by EELS. *Polymer* **1999**, 40, 5691–5697.
- (180) Sutter, E.; Jungjohann, K.; Bliznakov, S.; Courty, A.; Maisonhaute, E.; Tenney, S.; Sutter, P. In Situ Liquid-Cell Electron Microscopy of Silver-Palladium Galvanic Replacement Reactions on Silver Nanoparticles. *Nat. Commun.* **2014**, *5*, 4946.
- (181) Woehl, T. J.; Abellan, P. Defining the Radiation Chemistry during Liquid Cell Electron Microscopy to Enable Visualization of Nanomaterial Growth and Degradation Dynamics. *J. Microsc.* **2017**, 265, 135–147.
- (182) Thomas, J. K. Rates of Reaction of the Hydroxyl Radical. *Trans. Faraday Soc.* **1965**, *61*, 702–707.
- (183) Adams, G. E.; Armstrong, R. C.; Charlesby, A.; Michael, B. D.; Willson, R. L. Pulse Radiolysis of Sulphur Compounds. Part 3.—Repair by Hydrogen Transfer of a Macromolecule Irradiated in Aqueous Solution. *Trans. Faraday Soc.* 1969, 65, 732–742.
- (184) E Adams, B. G.; Mcnaughton, G. S.; Michael, B. D.; Adams, G. E.; Mcnaughton A N D B D Michael, G. S. Pulse Radiolysis of Sulphur Compounds. Part 2 Free Radical "Repair" by Hydrogen Transfer from Sulphydryl Compounds. *Trans. Faraday Soc.* 1968, 64, 902–910.
- (185) Ferry, M.; Ngono-Ravache, Y.; Aymes-Chodur, C.; Clochard, M. C.; Coqueret, X.; Cortella, L.; Pellizzi, E.; Rouif, S.; Esnouf, S. Ionizing Radiation Effects in Polymers. *In Reference Module in Materials Science and Materials Engineering* **2016**, 1–28.
- (186) Cosslett, V. E. Radiation Damage in the High Resolution Electron Microscopy of Biological Materials: A Review. *J. Microsc.* **1978**, *113*, 113–129.
- (187) Egerton, R. F.; Crozier, P. A.; Rice, P. ELECTRON ENERGY LOSS SPECTROSCOPY AND CHEMICAL CHANGE. *Ultramicroscopy* **1987**, 23, 305–312.
- (188) Egerton, R. F.; Takeuchi, M. Radiation Damage to Fullerite (C60) in the Transmission Electron Microscope. *Appl. Phys. Lett.* **1999**, 75, 1884–1886.
- (189) Grubb, D. T. Review Radiation Damage and Electron Microscopy of Organic Polymers. J. Mater. Sci. 1974, 9, 1715–1736.
- (190) Schulman, S. G. Fundamentals of Interaction of Ionizing Radiations with Chemical, Biochemical, and Phamaceutical Systems. *J. Pharm. Sci.* **1973**, *62*, 1745–1757.
- (191) Sedlacek, O.; Kucka, J.; Monnery, B. D.; Slouf, M.; Vetrik, M.; Hoogenboom, R.; Hruby, M. The Effect of Ionizing Radiation on Biocompatible Polymers: From Sterilization to Radiolysis and Hydrogel Formation. *Polym. Degrad. Stab.* **2017**, *137*, 1–10.
- (192) Vasile, C.; Butnaru, E. Radiation Chemistry of Organic Solids. In Applications of ionizing radiation in materials processing 2017, 117–141
- (193) Berger, M. J.; Seltzer, S. M. Stopping Powers and Ranges of Electrons and Positrons; National Bureau of Standards, U.S. Department of Commerce, 1982. DOI: 10.6028/NBS.IR.82-2550.
- (194) Gümüs, H. Simple Stopping Power Formula for Low and Intermediate Energy Electrons. *Radiat. Phys. Chem.* **2005**, 72, 7–12. (195) Sugiyama, H. Stopping Power Formula for Intermediate

Energy Electrons. Phys. Med. Biol. 1985, 30, 331-335.

- (196) Guillet, J. E.; Hesp, S. A. M.; Takeuchi, Y. Role of Excitation Transfer in the Photochemistry and Radiation Chemistry of Solid Polymers. *In Radiation Effects on Polymers* **1991**, 475, 414–431.
- (197) Cai, Z.; Chen, S.; Wang, L. W. Dissociation Path Competition of Radiolysis Ionization-Induced Molecule Damage under Electron Beam Illumination. *Chem. Sci.* **2019**, *10*, 10706–10715.
- (198) Isaacson, M.; Johnson, D.; Crewe, A. V. Electron Beam Excitation and Damage of Biological Molecules; Its Implications for Specimen Damage in Electron Microscopy. *Radiat. Res.* **1973**, *55*, 205.
- (199) Dyne, P. J. Charge Transfer and Electron Capture in the Radiolysis of Aliphatic Hydrocarbons. *Can. J. Chem.* **1965**, 43, 1080–1092.
- (200) Chapiro, A. General Consideration of the Radiation Chemistry of Polymers. *Nucl. Instrum. Methods Phys. Res., Sect. B* **1995**, *105*, 5–7.
- (201) Siangchaew, K.; Libera, M. The Influence of Fast Secondary Electrons on the Aromatic Structure of Polystyrene. *Philos. Mag. A* **2000**, *80*, 1001–1016.
- (202) Jungjohann, K. L.; Evans, J. E.; Aguiar, J. a.; Arslan, I.; Browning, N. D. Atomic-Scale Imaging and Spectroscopy for In Situ Liquid Scanning Transmission Electron Microscopy. *Microsc. Microanal.* **2012**, *18*, 621–627.
- (203) Zaluzec, N. J.; Burke, M. G.; Haigh, S. J.; Kulzick, M. a. X-Ray Energy-Dispersive Spectrometry During In Situ Liquid Cell Studies Using an Analytical Electron Microscope. *Microsc. Microanal.* **2014**, 20, 323–329.
- (204) Singh, P.; Venugopal, B. R.; Nandini, D. R. Effect of Electron Beam Irradiation on Polymers. *J. Mod. Mater.* **2017**, *5*, 24–33.
- (205) Varlot, K.; Martin, J. M.; Quet, C.; Kihn, Y. Towards Sub-Nanometer Scale EELS Analysis of Polymers in the TEM. *Ultramicroscopy* **1997**, *68*, 123–133.
- (206) Varlot, K.; Martin, J. M.; Quet, C. Physical and Chemical Changes in Polystyrene during Electron Irradiation Using EELS in the TEM: Contribution of the Dielectric Function. *J. Microsc.* **1998**, *191*, 187–194.
- (207) Ritsko, J. J. Electron Energy Loss Spectroscopy of Pristine and Radiation Damaged Polyethylene. *J. Chem. Phys.* **1979**, 70, 5343–5349.
- (208) Yakovlev, S.; Libera, M. Dose-Limited Spectroscopic Imaging of Soft Materials by Low-Loss EELS in the Scanning Transmission Electron Microscope. *Micron* **2008**, *39*, 734–740.
- (209) Swanson, N.; Powell, C. J. Excitation of π Electrons in Polystyrene and Similar Polymers by 20-KeV Electrons. *J. Chem. Phys.* **1963**, 39, 630–634.
- (210) Ritsko, J. J.; Bigelow, R. W. Core Excitons and the Dielectric Response of Polystyrene and Poly(2-Vinylpyridine) from 1 to 400 EV. *J. Chem. Phys.* **1978**, *69*, 4162–4170.
- (211) Egerton, R. F. Scattering Delocalization and Radiation Damage in STEM-EELS. *Ultramicroscopy* **2017**, *180*, 115–124.
- (212) Plis, E. A.; Engelhart, D. P.; Cooper, R.; Johnston, W. R.; Ferguson, D.; Hoffmann, R. Review of Radiation-Induced Effects in Polyimide. *Appl. Sci.* **2019**, *9*, 1–23.
- (213) Tabata, Y. Heterogeneous Nature of Radiation Effect on Polymers. In *Irradiation of Polymeric Materials*; American Chemical Society, 1993; pp 27–49.
- (214) Hill, D. J. T.; O'Donnell, J. H.; Pomery, P. J. Fundamental Aspects of Polymer Degredations by High-Energy Radiation. *In Materials for Microlithography* **1985**, 266, 125–149.
- (215) Lenhart, J. L.; Cole, P. J.; Cole, S. M.; Schroeder, J. L.; Belcher, M. E. Radiation Tolerant Polymeric Films through the Incorporation of Small Molecule Dopants in the Polymer Matrix. *J. Appl. Phys.* **2008**, *103*, 024908.
- (216) Ennis, C. P.; Kaiser, R. I. Mechanistical Studies on the Electron-Induced Degradation of Polymers: Polyethylene, Polytetra-fluoroethylene, and Polystyrene. *Phys. Chem. Chem. Phys.* **2010**, *12*, 14884–14901.
- (217) Ngono-Ravache, Y. Spectroscopic Study of Chemical Modifications Induced by Swift Heavy Ions on Polymers: The

- Contribution of the CIRIL Platform and the CIMAP Laboratory. J. Phys.: Conf. Ser. 2015, 629, 012006.
- (218) Helbert, J. N.; Poindexter, E. H.; Stahl, G. A.; Chen, C. Y.; Pittman, C. U. Radiation Degradation Susceptibility of Vinyl Polymers: Nitriles and Anhydrides. *J. Polym. Sci., Polym. Chem. Ed.* 1979, 17, 49–58.
- (219) Ashfold, M. N. R.; Ingle, R. A.; Karsili, T. N. V.; Zhang, J. Photoinduced C-H Bond Fission in Prototypical Organic Molecules and Radicals. *Phys. Chem. Chem. Phys.* **2019**, *21*, 13880–13901.
- (220) Pal, R.; Sikder, A. K.; Saito, K.; Funston, A. M.; Bellare, J. R. Electron Energy Loss Spectroscopy for Polymers: A Review. *Polym. Chem.* **2017**, *8*, 6927–6937.
- (221) Navarro, R.; Burillo, G.; Adem, E.; Marcos-Fernández, A. Effect of Ionizing Radiation on the Chemical Structure and the Physical Properties of Polycaprolactones of Different Molecular Weight. *Polymers (Basel, Switz.)* **2018**, *10*, 397.
- (222) O'Donnell, J. H. Chemistry of Radiation Degradation of Polymers. In Radiation Effects on Polymers 1991, 475, 402–413.
- (223) Zainuddin, Z.; Albinska, J.; Ulański, P.; Rosiak, J. M. Radiation-Induced Degradation and Crosslinking of Poly(Ethylene Oxide) in Solid State. *J. Radioanal. Nucl. Chem.* **2002**, 253, 339–344. (224) Dawes, K.; Glover, L. C.; Vroom, D. A. The Effects of Electron Beam and G-Irradiation on Polymeric Materials. *In Physical*
- Properties of Polymers Handbook 2007, 867–887. (225) Miller, A. A.; Lawton, E. J.; Balwit, J. S. Effect of Chemical Strucyture of Vinyl Polymers on Crosslinking and Degradation by Ionizaing Radiation. *J. Polym. Sci.* 1954, 14, 503–504.
- (226) Heiland, K.; Hill, D. J. T.; O'Donnell, J. H.; Pomery, P. J. Radiation Degradation of Poly(Arlene Ether Ketone)S. *Polym. Adv. Technol.* **1994**, *5*, 116–121.
- (227) Lyu, J.; Gong, X.; Lee, S.; Gnanasekaran, K.; Zhang, X.; Wasson, M. C.; Wang, X.; Bai, P.; Guo, X.; Gianneschi, N. C.; Farha, O. K. Phase Transitions in Metal Organic Frameworks Directly Monitored through In Situ Variable Temperature Liquid-Cell Transmission Electron Microscopy and In Situ X-ray Diffraction. *J. Am. Chem. Soc.* 2020, 142, 4609–4615.
- (228) Smith, B. J.; Parent, L. R.; Overholts, A. C.; Beaucage, P. A.; Bisbey, R. P.; Chavez, A. D.; Hwang, N.; Park, C.; Evans, A. M.; Gianneschi, N. C.; Dichtel, W. R. Colloidal Covalent Organic Frameworks. *ACS Cent. Sci.* **2017**, 3 (1), 58.
- (229) Yamazaki, T.; Kimura, Y.; Vekilov, P. G.; Furukawa, E.; Shirai, M.; Matsumoto, H.; Van Driessche, A. E. S.; Tsukamoto, K. Two Types of Amorphous Protein Particles Facilitate Crystal Nucleation. *Proc. Natl. Acad. Sci. U. S. A.* **2017**, *114*, 2154–2159.
- (230) Zhu, Y.; Ciston, J.; Zheng, B.; Miao, X.; Czarnik, C.; Pan, Y.; Sougrat, R.; et al. Unravelling Surface and Interfacial Structures of a Metal-Organic Framework by Transmission Electron Microscopy. *Nat. Mater.* **2017**, *16*, 532–537.
- (231) Wiktor, C.; Meledina, M.; Turner, S.; Lebedev, O. I.; Fischer, R. A. Transmission Electron Microscopy on Metal-Organic Frameworks-a Review. *J. Mater. Chem. A* **2017**, *5*, 14969–14989.
- (232) Schorb, M.; Haberbosch, I.; Hagen, W. J. H.; Schwab, Y.; Mastronarde, D. N. Software Tools for Automated Transmission Electron Microscopy. *Nat. Methods* **2019**, *16*, 471–477.
- (233) Wu, S.; Armache, J. P.; Cheng, Y. Single-Particle Cryo-EM Data Acquisition by Using Direct Electron Detection Camera. *Microscopy* **2016**, *65*, 35–41.
- (234) Li, X.; Mooney, P.; Zheng, S.; Booth, C. R.; Braunfeld, M. B.; Gubbens, S.; Agard, D. A.; Cheng, Y. Electron Counting and Beam-Induced Motion Correction Enable near-Atomic-Resolution Single-Particle Cryo-EM. *Nat. Methods* **2013**, *10*, 584–590.
- (235) Li, X.; Zheng, S. Q.; Egami, K.; Agard, D. A.; Cheng, Y. Influence of Electron Dose Rate on Electron Counting Images Recorded with the K2 Camera. *J. Struct. Biol.* **2013**, *184*, 251–260.
- (236) McMullan, G.; Faruqi, A. R.; Clare, D.; Henderson, R. Comparison of Optimal Performance at 300keV of Three Direct Electron Detectors for Use in Low Dose Electron Microscopy. *Ultramicroscopy* **2014**, *147*, 156–163.

- (237) Wang, C.; Qiao, Q.; Shokuhfar, T.; Klie, R. F. High-Resolution Electron Microscopy and Spectroscopy of Ferritin in Biocompatible Graphene Liquid Cells and Graphene Sandwiches. *Adv. Mater.* **2014**, *26* (21), 3410–3414.
- (238) Abellan, P.; Woehl, T. J.; Parent, L. R.; Browning, N. D.; Evans, J. E.; Arslan, I. Factors Influencing Quantitative Liquid (Scanning) Transmission Electron Microscopy. *Chem. Commun.* **2014**, *50* (38), 4873. .
- (239) Mehdi, B. L.; Stevens, A.; Kovarik, L.; Jiang, N.; Mehta, H.; Liyu, A.; Reehl, S.; Stanfill, B.; Luzi, L.; Hao, W.; Bramer, L.; Browning, N. D. Controlling the Spatio-Temporal Dose Distribution during STEM Imaging by Subsampled Acquisition: In-Situ Observations of Kinetic Processes in Liquids. *Appl. Phys. Lett.* **2019**, *115*, 063102.
- (240) Park, C.; Woehl, T. J.; Evans, J. E.; Browning, N. D. Minimum Cost Multi-Way Data Association for Optimizing Multitarget Tracking of Interacting Objects. *IEEE Trans. Pattern Anal. Mach. Intell.* 2015, 37, 611–624.
- (241) Bakalis, E.; Parent, L. R.; Vratsanos, M.; Park, C.; Gianneschi, N. C.; Zerbetto, F. Complex Nanoparticle Diffusional Motion in Liquid-Cell Transmission Electron Microscopy. *J. Phys. Chem. C* **2020**, *124*, 14881–14890.